The Innovative Design of Epicyclic Cam-Roller Trains: The Planar Case

TR-CIM-03.05 February, 2004

Xiang Zhang and Jorge Angeles

Centre for Intelligent Machines (CIM) and

Department of Mechanical Engineering

McGill University

Montreal, Quebec, Canada H3A 2K6

Abstract

The subject of the work reported here is the innovative design of epicyclic (planetary) cam-roller trains, intended for speed-reduction ratios higher than those obtained with simple trains of the Speed-o-Cam family, reported elsewhere. We limit ourselves in this report to planar trains. The kinematic relations of the mechanism with a given speed-reduction ratio are analyzed; accordingly, the profiles of the sun-cam and ring-cam, key elements of the mechanism, are obtained. Furthermore, the condition for undercutting-avoidance of the ring-cam is derived. For mechanical design, different layouts of the epicyclic cam-roller trains are discussed for the structure and transmission optimization, based on the pressure angle. Moreover, a static force analysis is reported, its aim being the prediction of failure of key parts, besides enabling the contact stress analysis of cam and rollers. Finally, a planetary cam-roller speed reducer is designed with Pro/E, with which drawings are produced for the prototype.

1 Introduction

Speed reduction is a very important topic nowadays. More and more new applications require different types of speed reducers. Transmission precision, efficiency, and simple structure are in high demand. Gear trains (Buckingham, 1963; Dudley, 1966) and planetary gear trains (Müller, 1971) have been researched and developed for this purpose, as well as harmonic drives (Yuen, 1996; Tuttle and Seering, 1993). However, these mechanisms have their shortcomings when used in applications, namely, complicated tooth profiles, backlash, low load-carrying capacity per tooth, low transmission stiffness, etc.

Speed-o-Cam (SoC), a speed-reduction mechanism based on cams and pure-rolling contact, as shown in Figs. 1 and 2, is currently under development at McGill University's Centre for Intelligent Machines. SoC is intended to replace gears and harmonic drives

Figure 1: Planar SoC train

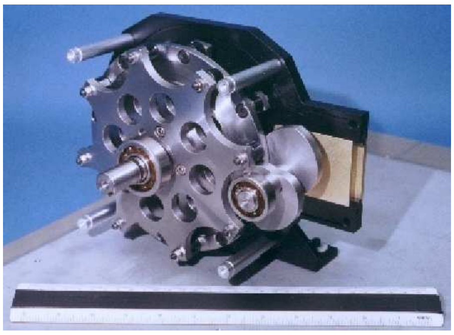

Figure 2: Prototype of a planar SoC

in applications where backlash, friction, and flexibility cannot be tolerated.

A cam-synthesis methodology was developed by González-Palacios and Angeles (1993) to design mechanisms with minimum sliding. This methodology then led to a family of speed reducers intended to replace gear trains by offering (González-Palacios and Angeles, 1999): high speed-reduction ratios, low friction losses, low backlash and high stiffness, besides the possibility of manufacturing with general-purpose CNC machine tools. Further studies towards the application of this kind of speed reducer are in progress.

The motivation of this project is the design and development of planetary cam-roller trains, so that a higher speed-reduction ratio can be realized, within acceptable variations of the pressure angle, than with a single-stage SoC transmission.

Let $i_{12} = \omega_1/\omega_2$; ω_1 and ω_2 are the angular velocities of shafts 1 and 2, respectively, with $i_{12} > 0$ if ω_1 and ω_2 are in the same direction; otherwise, $i_{12} < 0$. Likewise, $i = \omega_{\text{input}}/\omega_{\text{output}}$.

2 The Architecture of a Planetary Cam-Roller Train

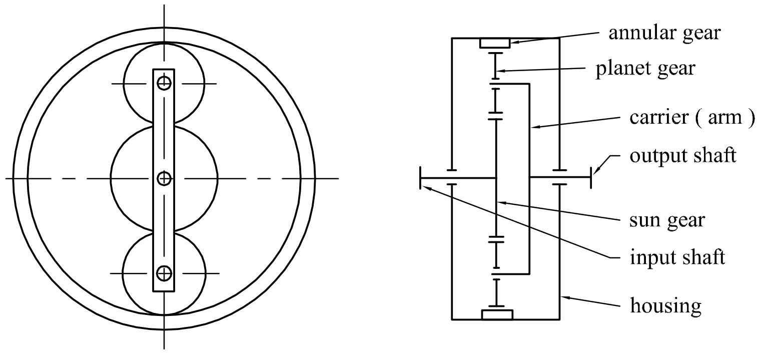

Figure 3: A planetary (epicyclic) gear train

A typical planetary (epicyclic) gear train, shown in Fig. 3, is composed of: the planet gears; the sun gear; the planet arm and the annular gear (ring gear). A planetary cam-

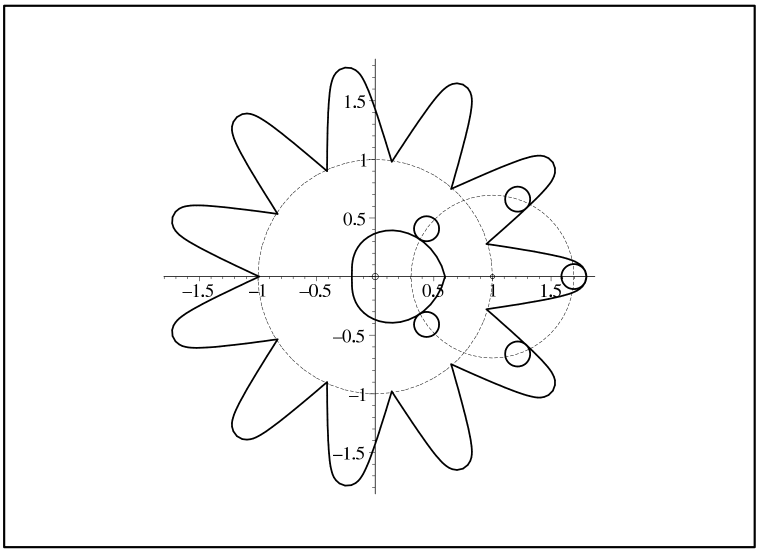

Figure 4: A planetary cam-roller train of the CDC type

roller train, in turn, has two possible layouts, as shown in Figs. 4 and 5. Figure 4 depicts a layout comprising a central external cam (EC or sun-cam), a planet roller-carying-disk

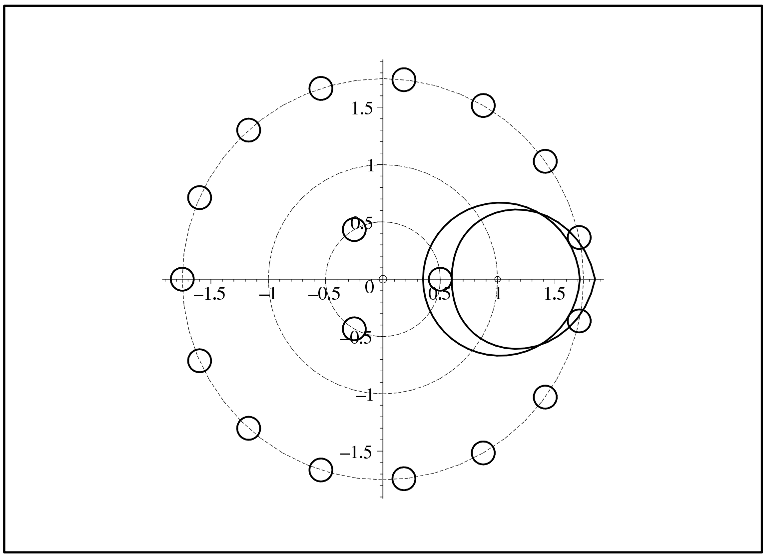

Figure 5: A planetary cam-roller train of the DCD type

(RCD) and an outer internal cam (IC or ring-cam). We shall call this layout CDC. In Fig. 5, in turn, a layout comprising a central RCD, a planet external cam and an outer RCD is illustrated. This layout will be termed DCD. Compared with the CDC layout, the DCD layout includes an inner and an outer RCD, which are simpler to fabricate; however, some disadvantages cannot be overlooked:

- lower speed-reduction ratio;
- the planetary cams are unbalanced;
- for the same speed-reduction ratio, the space required is much bigger than that required by the CDC type;

Accordingly, in this report only CDC layouts are studied. The advantages offered by CDC trains are listed below:

- The planet is a wheel with rollers mounted on it, which provides an inherent balance. If two or more planet wheels are considered, the whole planet-carrying-arm (PCA) is also inherently balanced;

- The speed-reduction ratio is high when compared with a typical planetary gear train shown in Fig. 3, because the sun-cam can be considered as a single tooth gear;

- The thickness is small when compared with DCD layouts;

- If the rollers are designed as the weakest link of the whole train, the expensive sun-cam and ring-cam can thus be designed for a longer life; only the relatively low-cost rollers will need periodical replacement;

- Notice that the speed-reduction ratio can be changed by changing different number of lobes of the ring-cam, while keeping the outside dimension of the ring-cam unchanged.

We summarize below the foregoing terminology:

- The sun-cam is the input shaft.

- The ring-cam, or annular cam, is fixed to the ground.

- The roller-carrying-disk (RCD), carries the rollers that engage with the sun-cam and the ring-cam.

- The planet-carrying arm (PCA) is the output shaft; it carries the RCDs.

- N: For the CDC train, N represents the number of rollers of each RCD.

- M: For the CDC train, M represents the number of lobes of the ring-cam.

3 The Determination of the Cam Profile

For a planar SoC train, the cam profile can be obtained by using the methodology of González-Palacios and Angeles (1999). As shown in Fig. 6, the Cartesian coordinates of

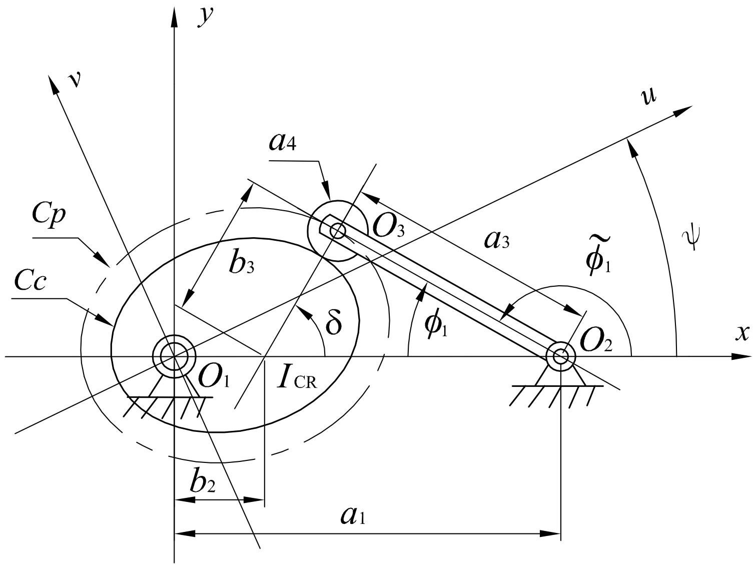

Figure 6: A planar cam-roller train

the cam profile for planar SoC in the u-v plane are:

$$u(\psi) = b_2 \cos\psi + (b_3 - a_4)\cos(\psi - \delta) \tag{1a}$$

$$v(\psi) = -b_2 \sin\psi - (b_3 - a_4)\sin(\psi - \delta) \tag{1b}$$

where

$$b_2 = \frac{\tilde{\phi}'}{\tilde{\phi}' - 1} a_1 \tag{2a}$$

$$b_3 = \sqrt{(a_3 \cos\tilde{\phi} + a_1 - b_2)^2 + (a_3 \sin\tilde{\phi})^2} \tag{2b}$$

$$\delta = \arctan\left(\frac{a_3 \sin\tilde{\phi}}{a_3 \cos\tilde{\phi} + a_1 - b_2}\right) \tag{2c}$$

For the external planar SoC, the relationship of the input-output angles of rotation takes the form:

$$\tilde{\phi} = \pi\left(1 - \frac{1}{N}\right) + \frac{\psi}{N} \tag{3a}$$

while the external planar SoC entails an input-output relationship of the form:

$$\tilde{\phi} = -\left[\pi\left(1 - \frac{1}{N}\right) + \frac{\psi}{N}\right] \tag{3b}$$

The notation used here is described below:

- C_c : cam profile;
- C_p : pitch curve;
- a_1 : distance between the input and output axis;
- a_3 : distance between the output and roller axis;
- a_4 : radius of the roller;
- N : the number of rollers in a planar SoC speed reducer;
- ψ : angular displacement of the cam;

- $\tilde{\phi}$: angular displacement of the follower arm;

- $\tilde{\phi}'$: $d\tilde{\phi}/d\psi$.

We define, moreover,

- $\bar{a}_i = a_i/a_1$, $i = 3, 4$, a dimensionless parameter, and

- $\bar{u}$, $\bar{v}$: nondimensional coordinates of the cam profile.

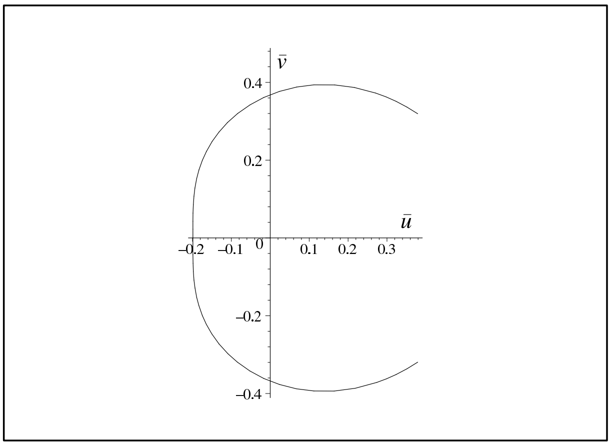

Figure 7: Cam profile in $0 \leq \psi \leq 2\pi$

Figure 7 shows the profile of a cam with $\bar{a}_3 = 0.694400$, $\bar{a}_4 = 0.106667$, $N = 5$ and $0 \leq \psi \leq 2\pi$, in which the profile does not close. An *extended angle* Δ is introduced so that the cam profile can be closed with $-\Delta \leq \psi \leq 2\pi + \Delta$. Angle Δ is obtained as a root of the equation:

$$v(-\Delta) = 0 \tag{4}$$

By solving the equation, the extension angle Δ can be obtained. Thus, the cam profile is determined from eq.(1) when ψ changes from $\psi_{min} \leq \psi \leq \psi_{max}$. Notice that:

$$\psi_{\min} = -\Delta \tag{5a}$$

$$\psi_{\max} = 2\pi + \Delta \tag{5b}$$

For a CDC train, like that of Fig. 4, the cam profile can also be obtained using the above relations. This is reasonable because when an angular velocity is given to the planetary system which is equal to the angular velocity of planetary arm, but in the opposite direction, the planetary arm angular velocity becomes 0, the given CDC train now changes to two planar SoC mechanisms, one being external, the other internal.

For the external SoC train, by using the relations recalled above, the profile of the sun-cam can be readily obtained. Table 1 includes the dimensionless coordinates of the

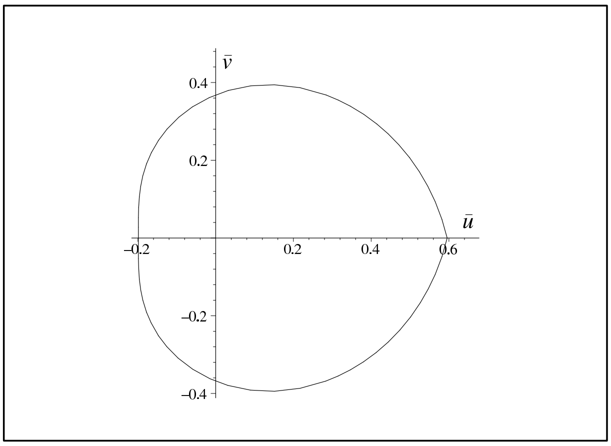

Figure 8: A cam profile with $\bar{a}_3 = 0.694400$, $\bar{a}_4 = 0.106667$ and $N = 5$

points on the cam profile and the value of the extension angle Δ, for the cam of Fig. 8. For the internal SoC train, likewise, only the profile for one lobe of the ring-cam is

Table 1: The nondimensional coordinates and extension angle Δ of a sun-cam profile

Profile points	$\bar{u}$	$\bar{v}$
1	0.595587	0.000000
2	0.361978	−0.330240
3	0.055533	−0.385456
4	−0.134724	−0.268617
5	−0.193755	−0.127538
6	−0.198933	0.000000
7	−0.193755	0.127538
8	−0.134724	0.268617
9	0.055533	0.385456
10	0.361978	0.330240
11	0.595587	0.000000
Δ (rad)	0.732136	

obtained, as shown in Fig. 9. The relations between the input and output angles in this case are:

$$\phi = \pi\left(1 + \frac{1}{N}\right) - M\frac{\psi}{N} \tag{6a}$$

$$\tilde{\phi} = -\pi\frac{1}{N} + M\frac{\psi}{N} \tag{6b}$$

$$b_{2\mathrm{rc}} = a_1\frac{\tilde{\phi}'}{\tilde{\phi}' - 1} = a_1\frac{M}{M - N} \tag{6c}$$

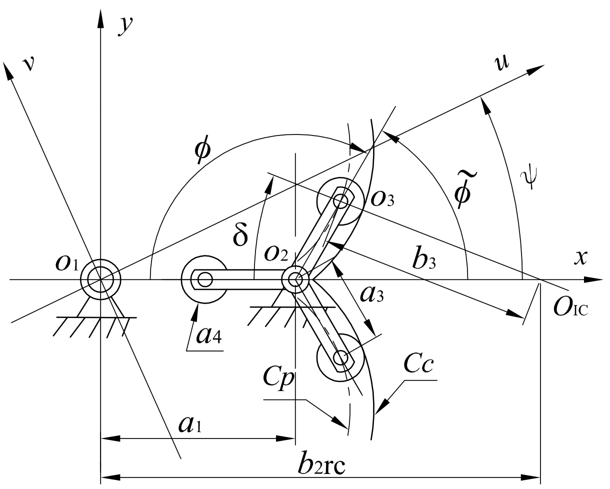

Figure 9: Ring-cam profile calculation with $\bar{a}_3 = 0.694400$, $\bar{a}_4 = 0.106667$ and $N = 3$

For other relations, please refer to eqs.(1) and (2). In this way, the profile of the lobes of the ring-cam is obtained. Figure 4 shows the whole profile of a ring-cam. Figure 10 shows three lobes of a ring-cam; notice that the first lobe is shown with a solid line, the other two with dashed line. Table 2 lists the dimensionless coordinates of eleven points and the extension angle of the first lobe of Fig. 10. Notice that, if the extension angle is not taken into consideration, the lobe profile will be incomplete. Figure 11 shows the incomplete lobe profile of the first lobe of Fig. 10, in which the solid line is the incomplete profile and the dashed line is the whole lobe profile, as computed using the extension angle Δ. For the first lobe, ψ changes from $-\Delta$ to $\Delta + 2\pi/M$. Figure 12 shows the whole profile of a ring-cam in the CDC trains of Fig. 9. By varying ψ from 0 to 24π, the whole profile of the ring-cam is obtained. However the inner part lines of the profile should be removed.

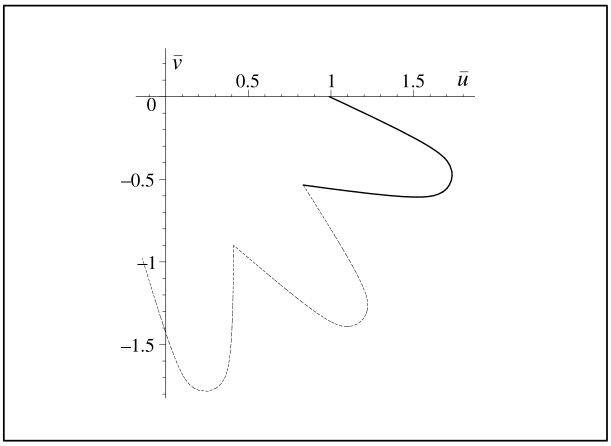

Figure 10: Profile of the lobes of a ring-cam with $\bar{a}_3 = 0.694400$, $\bar{a}_4 = 0.106667$, $N = 5$, $M = 11$

There is an alternative method to calculate the sun-cam profile. In this method, there is no need to 'fix' the PCA first. From Fig. 13, for the given CDC train, the notation used here is

- C_c : cam profile;
- a_1 : the length of the planetary arm, or the radius of the PCA;
- a_3 : the radius of the RCD;
- a_4 : the radius of the roller;
- O_1 : the joint centre of the sun-cam and PCA;
- O_2 : the joint centre of the RCD and PCA;
- O_3 : the joint centre of the roller and RCD;

Table 2: The nondimensional coordinates and the extension angle Δ of a lobe profile of a ring-cam

Profile points	$\bar{u}$	$\bar{v}$
1	0.989292	0.000000
2	1.227395	−0.111989
3	1.423791	−0.208576
4	1.572087	−0.288940
5	1.673422	−0.358915
6	1.728111	−0.507419
7	1.601816	−0.602782
8	1.478737	−0.606862
9	1.310534	−0.594294
10	1.093096	−0.569368
11	0.832245	−0.534852
Δ (rad)	0.624597	

- I_{CR} : the instant centre of the sun-cam w.r.t. the RCD;
- b_2 : the distance between O_1 and I_{CR};
- b_3 : the distance between O_3 and I_{CR};
- N : the number of rollers on each RCD;
- ψ : angular displacement of the sun-cam;

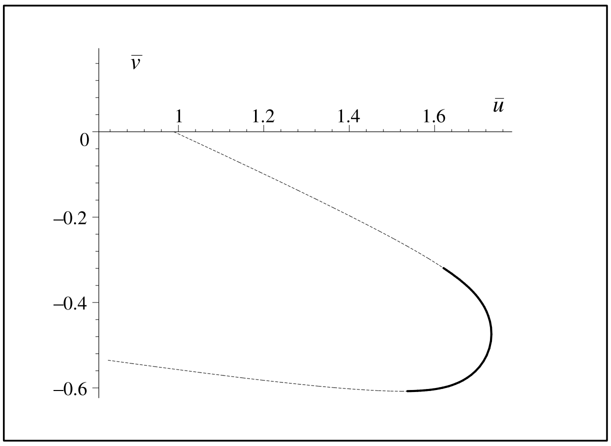

Figure 11: The incomplete lobe profile

- ψ_1 : angular displacement of the sun-cam w.r.t. the PCA;
- ψ_2 : angular displacement of the PCA w.r.t. the ground;
- ϕ_1 : angular displacement of the RCD w.r.t. the PCA;
- $\tilde{\phi}_1$: by definition, $\tilde{\phi}_1 = \pi - \phi_1$;
- δ : the angular displacement of the line $\overline{I_{\mathrm{CR}}O_3}$ w.r.t. the PCA.

For a given speed reduction ratio i, the PCA angular displacement ψ_2 and the angular displacement ψ_1 of the sun-cam respect to the PCA obey the relations:

$$\psi_2 = \psi/i \tag{7a}$$

$$\psi_1 = \psi - \psi_2/i \tag{7b}$$

When using eqs.(1), (2) and (3) to calculate the coordinates of the points of the sun-cam profile, ψ should be replaced by ψ_1. Also notice that this is an external train by

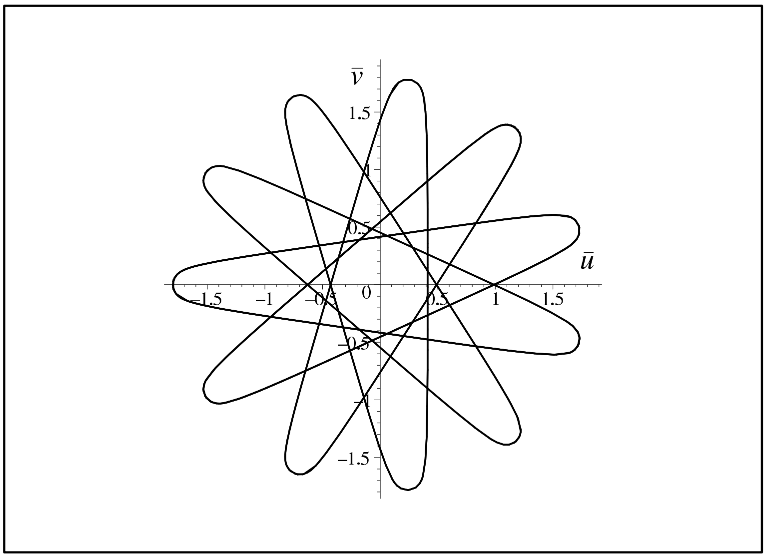

Figure 12: The profile of a ring-cam with $\bar{a}_3 = 0.694400$, $\bar{a}_4 = 0.106667$, $N = 5$ and $M = 11$

definition (Lee, 2001), so that the relations below applies:

$$\tilde{\phi}_1 = \pi\left(1 - \frac{1}{N}\right) + \frac{\psi_1}{N} \tag{8}$$

the sun-cam profile then being determined by the profile-point coordinates (u, v), namely,

$$u(\psi_1) = b_2 \cos\psi_1 + (b_3 - a_4)\cos(\psi_1 - \delta) \tag{9a}$$

$$v(\psi_1) = -b_2 \sin\psi_1 - (b_3 - a_4)\sin(\psi_1 - \delta) \tag{9b}$$

where:

$$b_2 = \frac{\tilde{\phi}_1'}{\tilde{\phi}_1' - 1} a_1 \tag{10a}$$

Notice that $\tilde{\phi}_1' = d\tilde{\phi}_1/\psi_1$. Moreover,

$$b_3 = \sqrt{(a_3 \cos\tilde{\phi}_1 + a_1 - b_2)^2 + (a_3 \sin\tilde{\phi}_1)^2} \tag{10b}$$

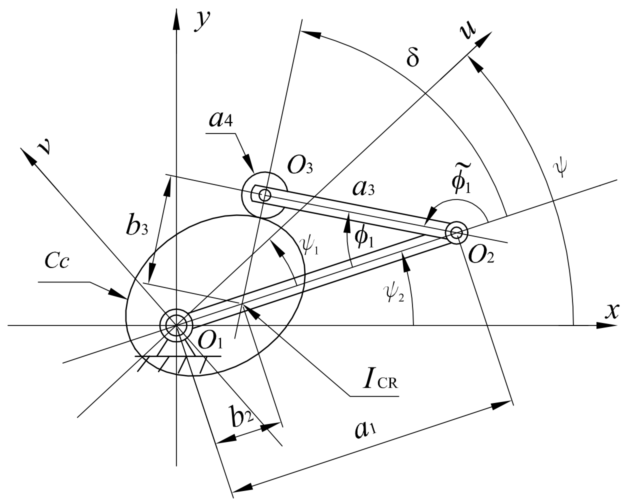

Figure 13: A planetary cam-roller train of the CDC type

$$\delta = \arctan\left(\frac{a_3 \sin\tilde{\phi}_1}{a_3\cos\tilde{\phi}_1 + a_1 - b_2}\right) \tag{10c}$$

Equations (8), (9) and (10) can be used to find the profile of the sun-cam now. Notice that ψ_1 is a function of ψ, and hence u, v, b_2, b_3 and δ are all functions of ψ. When ψ changes from 0 to 2π, only a part of the sun-cam profile can be obtained, as displayed in Fig. 14. By solving eq.(4) two roots can be obtained in the interval $[-\pi, 3\pi]$, namely,

$$r_{1\Delta} = 0.798694 \tag{11a}$$

$$r_{2\Delta} = -7.653078 \tag{11b}$$

Let:

$$\Delta_1 = r_{1\Delta} = 0.798694 \tag{12a}$$

$$\Delta_2 = -r_{2\Delta} = 7.653078 \tag{12b}$$

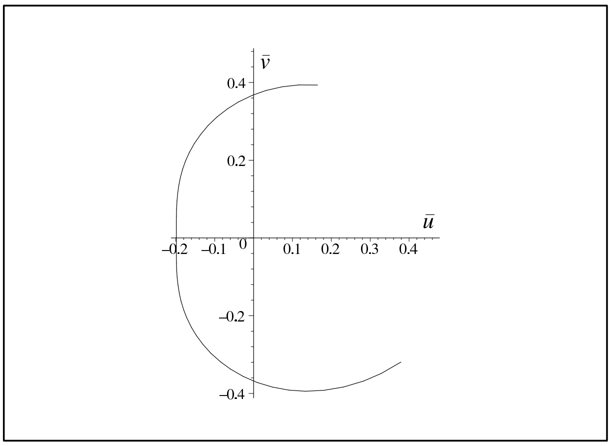

Figure 14: Partial profile of a sun-cam with $\bar{a}_3 = 0.649900$, $\bar{a}_4 = 0.106667$, $N = 5$ and $M = 11$

Now, the two extension angles Δ_1 and Δ_2 are available from eq.(12). Here, Δ_2 is lager than Δ_1, the difference being

$$\Delta_{21} \equiv \Delta_2 - \Delta_1 = 6.854384 \tag{13}$$

Moveover, notice that

$$\frac{2\pi}{M} + \Delta_1 + 2\pi = 7.653078 = \Delta_2 \tag{14}$$

the relation between Δ_1 and Δ_2 thus being:

$$\Delta_2 = \Delta_1 + \frac{2\pi}{M} + 2\pi \tag{15}$$

According to eq.(15), the number of lobes of a ring-cam and the extension angles are related by

$$M = \frac{2\pi}{\Delta_2 - \Delta_1 - 2\pi} \tag{16}$$

Table 3: The nondimensional coordinates and extension angles of a sun-cam profile

Profile points	$\bar{u}$	$\bar{v}$
1	0.595587	0.000000
2	0.361978	-0.330240
3	0.055533	-0.385456
4	-0.134724	-0.268617
5	-0.193755	-0.127538
6	-0.198933	0.000000
7	-0.193755	0.127538
8	-0.134724	0.268617
9	0.055533	0.385456
10	0.361978	0.330240
11	0.595587	0.000000
Δ_1 (rad)	0.798694	
Δ_2 (rad)	7.653078	

Table 3 shows that, for the same CDC train of Fig. 13, the sun-cam profile obtained is the same as that recorded in Table 1. However, the extension angles are different, which is due to the planetary motion of the PCA.

4 Speed-Reduction Ratio and Undercutting Conditions

The main purpose of CDC trains is to realize a higher speed-reduction ratio. A speed reduction analysis for CDC trains is thus necessary.

4.1 Speed-Reduction Ratio for a Simple Planar SoC

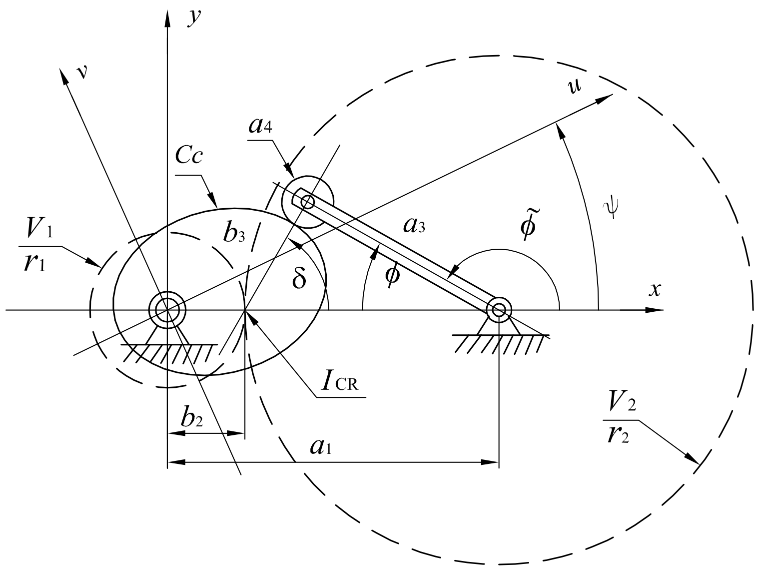

Figure 15: The virtual disk of a planar SoC

For a better analysis and understanding of the relative motions of the given train, virtual disks (VDs) are introduced, the engaging of the cam and the rollers then being replaced by that of the VDs. Figure 15 shows the VDs of a planar cam-roller train. Notice that point $I_{\rm CR}$ is the instant centre of the cam w.r.t. the follower-arm. The VD for the cam is the V_1 circle of radius r_1 centred at the cam centre of rotation, the VD for the follower-arm is the circle V_2 of radius r_2 centred at the follower-arm joint cnetre. Both V_1 and V_2 pass through point I_{CR}. At point I_{CR}, as Fig. 16 shows, the contact point of cam

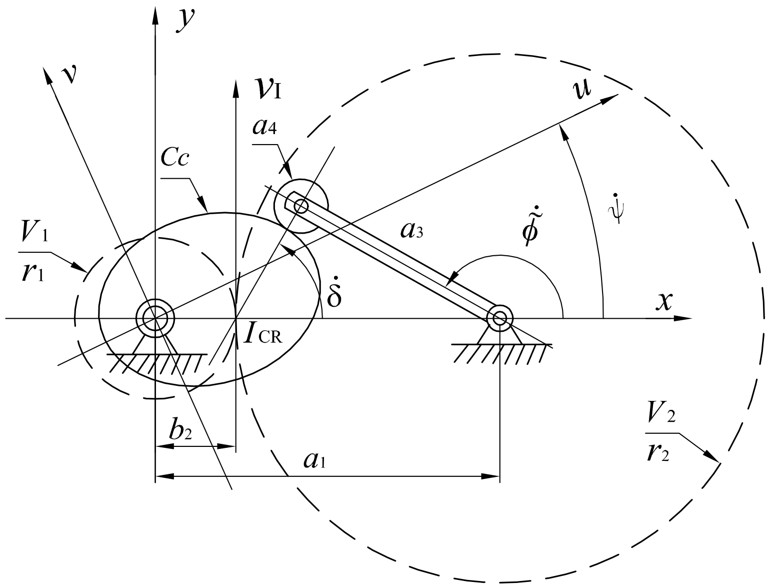

Figure 16: Virtual Disk of a planer cam-roller trains

and follower-arm have the same speed v_{I}. Thus, the motion transmission of the given cam-roller train is equal to the motion transition of two engaged gears with the pitch circles V_1 and V_2. According to Fig. 16, then, we obtain the relations:

$$r_1 = b_2 \tag{17a}$$

$$r_2 = a_1 - b_2 \tag{17b}$$

Thus, for the speed-reduction ratio i, we have:

$$i = \frac{r_2}{r_1} = \frac{a_1 - b_2}{b_2} \tag{18}$$

Takeing eqs.(2a) and (3b) into consideration, we obtain:

$$\phi' = -\frac{1}{N} \tag{19a}$$

$$b_2 = a_1 \frac{\phi'}{\phi' - 1} = a_1 \frac{1}{1+N} \tag{19b}$$

Thus, i can be obtained as:

$$i = \frac{a_1 - b_2}{b_2} = N \tag{20}$$

Which is a constant. Notice that i is determined only by the number of rollers, and has no direct relation with the other geometric parameters. Thus, for a given planar SoC, the speed reduction ratio i is understood as N.

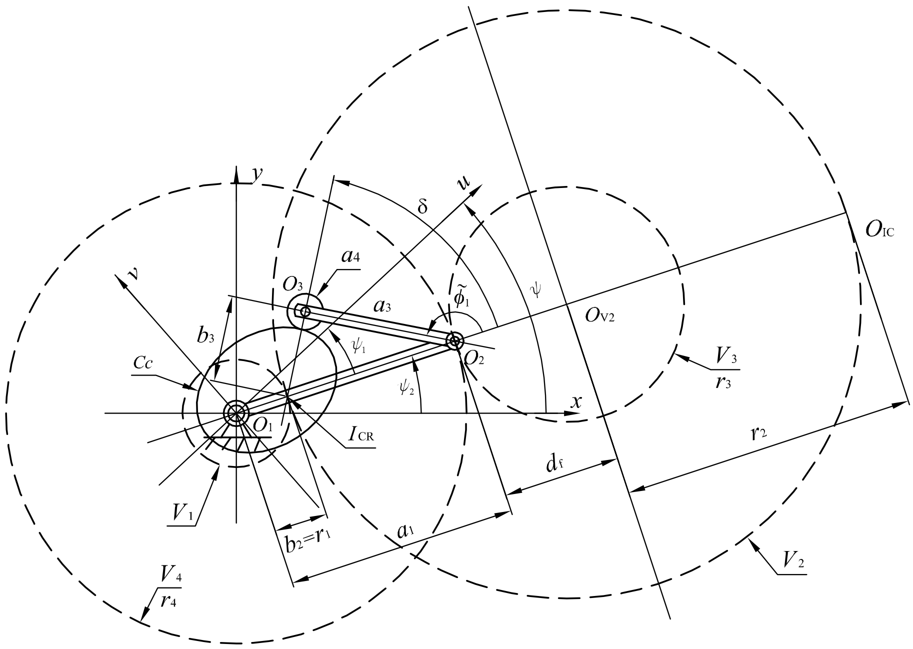

Figure 17: Virtual engaging disk of a CDC train

4.2 Speed-Reduction Ratio for CDC Trains

For CDC trains, the speed-reduction ratio i can be obtained also by using the VD concept. As Fig. 17 shows, the notation here is:

- V_1 : VD of the sun-cam with radius r_1;
- V_2 : VD of the RCD with radius r_2;
- V_3 : VD of the RCD with radius r_3;
- V_4 : VD of the PCA with radius r_4;
- O_{V2} : the centre of V_2;
- O_{IC} : the instant centre of the RCD or V_2 w.r.t. the ground or ring-cam;
- r_1 : the distance between O_1 and I_{CR}, or b_2, the radius of V_1;
- r_2 : the distance between O_{V2} and O_{IC}, i.e., the radius of V_2;
- r_3 : the distance between O_2 and O_{V2}, or d_{f}, the radius of V_3;
- r_4 : the distance between O_1 and O_2, or a_1, the radius of V_4;
- d_{f} : the distance between O_2 and O_{V2}, equal to $r_1 + r_2 - a_1$.

The notation is illustrated in Fig. 13. As with the planar SoC train, shown in Fig. 18, notice that:

- v_{V2} : the speed of O_{V2};

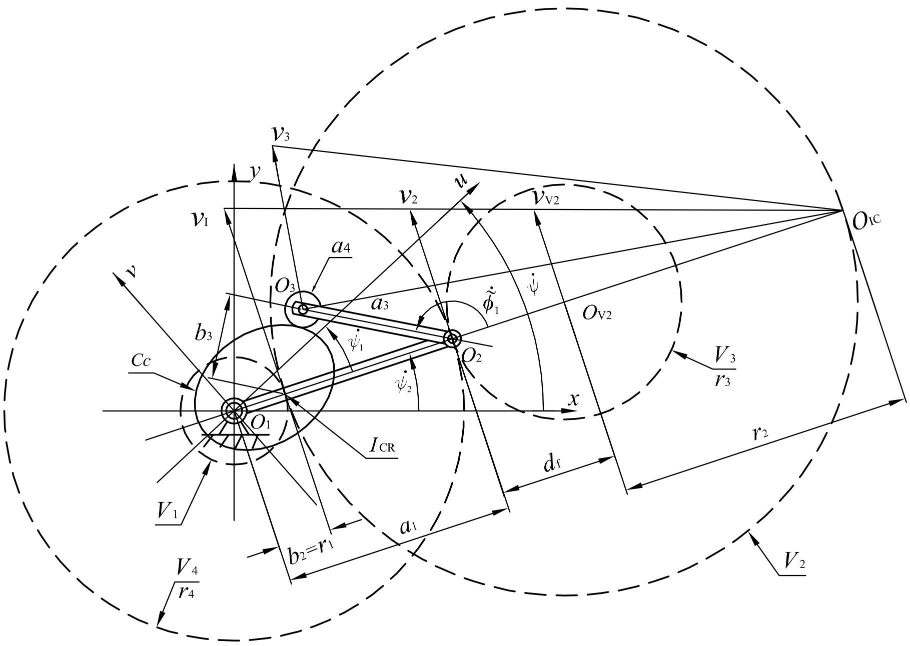

Figure 18: Speed relations of a CDC train

- v_2 : the speed of O_2;
- v_3 : the speed of O_3;
- v_I : the speed of the instant centre I_CR of the sun-cam w.r.t. the RCD.

Now, the speed reduction ratio i of a given CDC train can be obtained as described below:

According to Figs. 9 and 18, O_IC is apparently the instant centre of the ring-cam w.r.t. the RCD. Furthermore, from eqs.(2a) and (6), we obtain:

$$\overline{O_1 O_\mathrm{IC}} = b_{2\mathrm{rc}} = a_1 \frac{M}{M-N} \tag{21}$$

Thus, i can also be expressed as:

$$\begin{aligned} i = \frac{\omega_{\text{suncam}}}{\omega_{\text{PCA}}} = \frac{v_{\text{I}}}{r_1}\frac{a_1}{v_2} = \frac{v_{\text{I}}}{r_1}\frac{a_1}{v_{\text{I}}}\frac{\left(\overline{O_1 O}_{\text{IC}} - r_1\right)}{\left(\overline{O_1 O}_{\text{IC}} - a_1\right)} \\ = \frac{a_1}{b_2}\frac{\left(\overline{O_1 O}_{\text{IC}} - b_2\right)}{\left(\overline{O_1 O}_{\text{IC}} - a_1\right)} = M + 1 \end{aligned} \tag{22}$$

Which means that i, the speed-reduction ratio of the given CDC train, only depends on M, the number of the lobes of the ring-cam, and is independent of the geometric parameters. The speed-reduction ratio i of a given CDC train can be changed by changing only the number of the lobes of the ring-cam. The change will have no influence on other parts of the given CDC train. This advantage can be used to develop a 'speed shift' system, so that additional speed-reduction ratios can be realized.

4.3 Undercutting Condition

The undercutting condition for the cam in a planar SoC train was given by Lee (2001); it is applied here to the sun-cam of the CDC train. The main consideration here is the undercutting condition of the profile of the lobes of a ring-cam. Now, from Figs. 9 and 18, and eq.(21), O_{IC} is the instant centre of the RCD w.r.t. the ring-cam. Since the ring-cam is fixed on the ground, O_{IC} can be understood as the instant center of the RCD w.r.t. the ground. Furthermore, notice that, if $d_{\text{f}} = 0$ in Fig. 18, O_2, the joint centre of the RCD, and O_{V2}, the centre of V_2, coincide, and the roller centre O_3 must thus lie on V_2. This means that the roller centre O_3 must pass through the instant centre O_{IC} at some time. When this situation occurs, O_3 will lose either the tangential component or the normal component of its velocity, this point thus becoming a singular point on its trajectory. Figure 19 shows the foregoing condition, the trajectory of O_3 (dashed line in

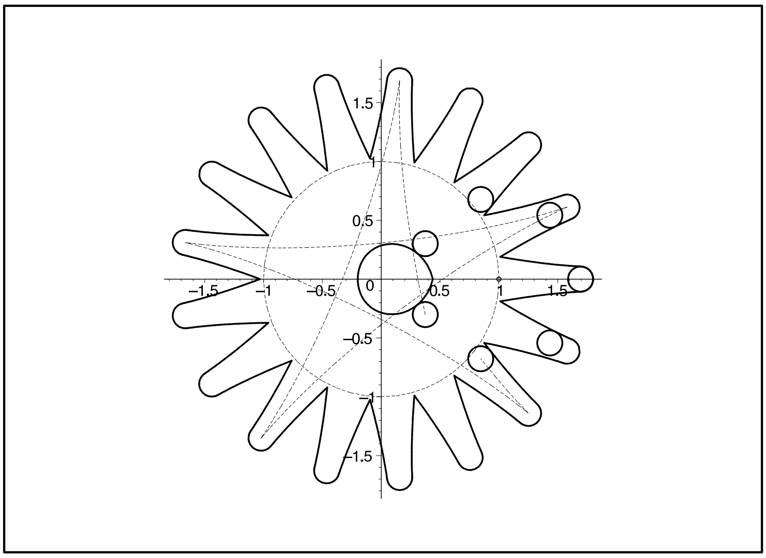

Figure 19: Critical condition of a CDC train with $\bar{a}_3 = 0.649900$, $\bar{a}_4 = 0.106667$, $N = 7$, $M = 17$

the figure), known as the pitch curve of the lobes, has a cusp in the middle of each lobe. This means that the velocity of O_3 at this configuration vanishes. Also, the profiles of the lobes reach their critical condition. Now we derive the undercutting condition. For the critical condition, from eq.(6c), we have

$$\begin{aligned} \overline{O_1 O_{\mathrm{IC}}} &= a_1 + a_3 \\ a_1 \frac{M}{M-N} &= a_1 + a_3 \\ M &= N \frac{a_1 + a_3}{a_3} \end{aligned} \tag{23}$$

Figure 20 shows a lobe profile (solid line) and its pitch curve (dashed line) when $M = N(a_1+a_3)/a_3$, the profile of the lobes of the ring-cam then reaching its critical condition.

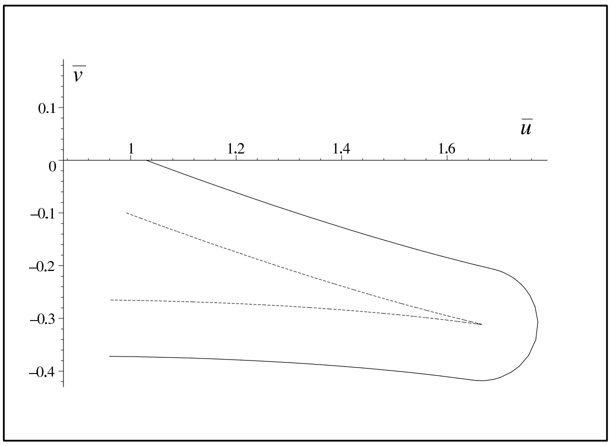

Figure 20: Critical condition of a ring-cam lobe with $\bar{a}_3 = 0.649900$, $\bar{a}_4 = 0.106667$, $N = 7$, $M = 17$

Notice here that $\bar{a}_3 = 0.649900$, $\bar{a}_4 = 0.106667$, $N = 7$, $M = 17$ and $i = 18$. For Fig. 20, if the number of lobes M increases to 18, the speed-reduction ratio i is now 19, and undercutting of the lobe profile then occurs. Figure 21 shows the lobe pitch curve (dashed line) and the lobe profile (solid line), which is impossible to machine.

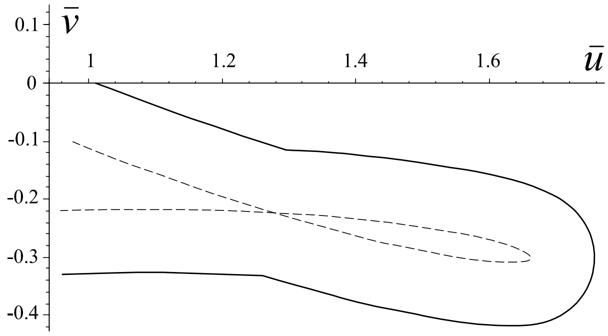

Figure 21: Undercutting of a ring-cam lobe with $\bar{a}_3 = 0.649900$, $\bar{a}_4 = 0.106667$, $N = 7$, $M = 18$

4.4 Summary of the Relations Between M and i

Based on the above analysis, we conclude that [1]:

- For a given CDC train, the speed-reduction ratio i depends on the number of lobes M of the ring-cam, and $i = M + 1$;
- The number of lobes M can vary from 1 to $\lfloor N(a_1 + a_3)/a_3 \rfloor$; when $M \geq \lfloor N(a_1 + a_3)/a_3 \rfloor$, then the critical or undercutting condition occurs on the lobe profile;
- $M = N$ is a special condition, under which the RCD moves with pure translation, the instant centre of the RCD thus lying at infinity. The profile should then be calculated by other method.

We can conclude that, with the same architecture, we can obtain a wide range of speed-reduction ratios from 2 to 13 for the CDC train shown in Fig. 13. Of course, different numbers of lobes of the ring-cam are needed for different reduction ratio.

5 Pressure Angle and Static Force Analysis

5.1 Pressure Angle Analysis

For a given CDC train, the force transmission chain is:

- From the sun-cam (input) to

[1] We use below the "floor function" $\lfloor \cdot \rfloor$, defined as the largest integer smaller than the real $(\cdot)$.

- the RCD (or RCDs), to
- the PCA (output).

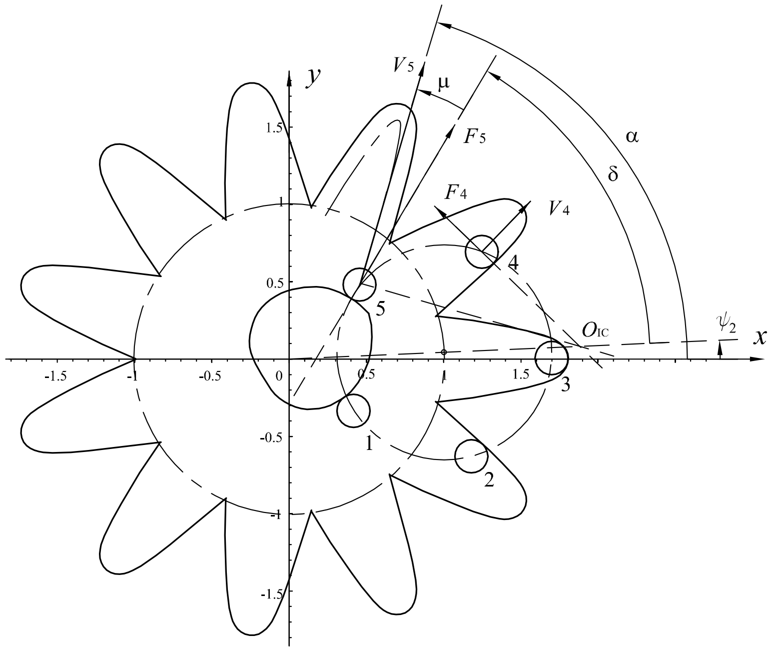

Figure 22: Force transmission of a CDC train

Figure 22 shows the force transmission of a CDC train with structural parameters $\bar{a}_3 = 0.649900$, $\bar{a}_4 = 0.106667$, $N = 5$ and $M = 11$, in which the notation is:

- F_{i} : contact force exerted by the sun-cam on the ith roller in contact;
- V_{i} : the speed of the centre of the ith roller in contact;
- μ : the pressure angle;
- α : the angle made by the speed V_{i} with the x axis, i.e., the angle made by the trajectory of the contact roller-centre;

Notice that, for roller No. 4, the contact force is F_4, which is perpendicular to the speed V_4. F_4 thus has no contribution to the motion of the RCD; it is a constraint force. So are the contact forces between roller No. 2 and No. 3 and the ring-cam.

As shown in Fig. 22, μ is the pressure angle. The calculations applicable to a planar SoC train were given in by Lee (2001). For the CDC train at hand, the equations for the calculation of μ are:

$$\frac{dy}{dx} = \tan\alpha$$
$$\alpha = \arctan\left(\frac{dy}{dx}\right) \tag{24a}$$

in which, x and y are the coordinates of a point of the trajectory of the roller centre, which are given in parametric form with the input angular displacement ψ as the parameter. Notice in Fig. 22, the relations:

$$\alpha = \mu + \delta + \psi_2$$
$$\mu = \alpha - \delta - \psi_2 \tag{24b}$$

the pressure angle thus being completely determined. From eqs.(7a), (10c) and (24a), it is apparent that μ is a function of $\bar{a}_3$, N, M and ψ, i.e.,

$$\mu = f(\bar{a}_3, N, M, \psi) \tag{25}$$

For optimization purposes, the influence of $\bar{a}_3$, N, M and ψ on μ is studied.

Firstly, the influence of $\bar{a}_3$ on μ can be represented by the curves of $\bar{a}_3$ and μ while N and M are fixed. Figure 23 shows, for different values of $\bar{a}_3$, the trends of the variation

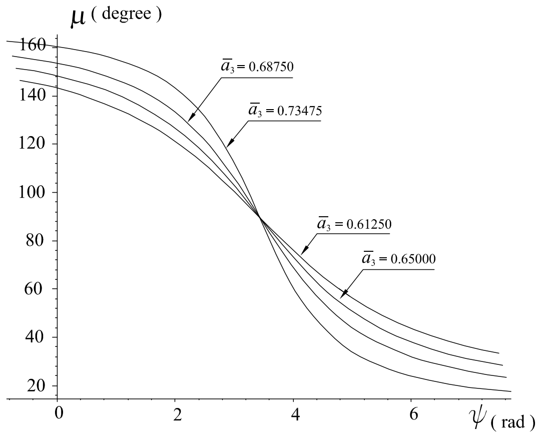

Figure 23: Pressure angle variation with $N = 6$ and $M = 11$

of μ w.r.t. $\bar{a}_3$. Notice that, as $\bar{a}_3$ increases, μ decreases. But $\bar{a}_3$ cannot be too high (Lee, 2001). In this case, $\bar{a}_3 = 0.73475$ is near the critical condition for a convex sun-cam. If $\bar{a}_3$ keeps increasing, the sun-cam will become concave and the machinability (Lee, 2001) will be low. Furthermore, an even higher $\bar{a}_3$ will induce undercutting of the profile of the sun-cam. On the other hand, a lower $\bar{a}_3$ will cause a higher pressure angle, which will cause a lower transmission efficiency.

As a compromise, in the final design, $\bar{a}_3 = 0.65$ was chosen, with $a_1 = 80$ mm and $a_3 = 55$ mm. With these parameters, the undercutting and low machinability of the sun-cam can be avoided while the values of the pressure angle are acceptable.

Secondly, for the influence of N on the pressure angle μ while $\bar{a}_3$ and M are fixed, as Fig. 24 shows, we have:

- The higher N, the higher μ is;

- A lower N can cause low machinability or even undercutting of the sun-cam (Lee,

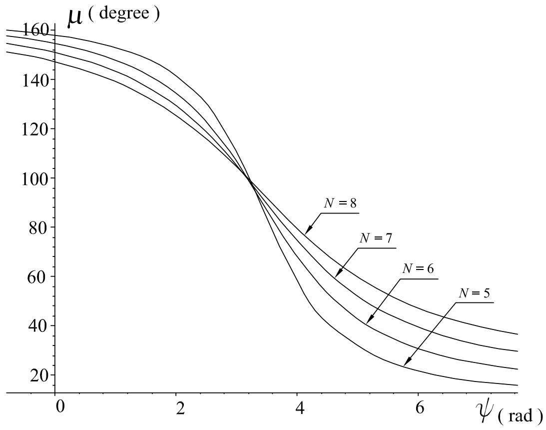

Figure 24: Pressure angle variation with $\bar{a}_3 = 0.6944$ and $M = 11$

2001).

In the final design, $N = 6$ was chosen.

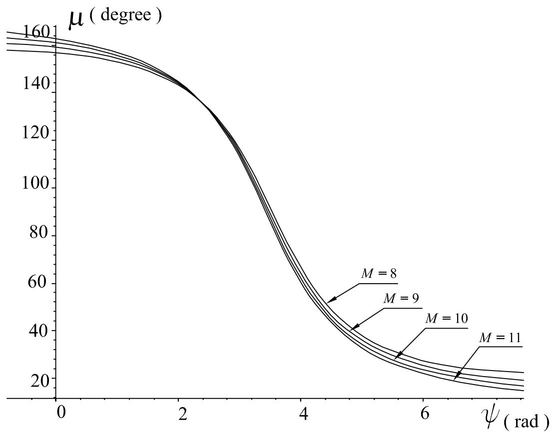

Figure 25: Pressure angle variation with $\bar{a}_3 = 0.6944$ and $N = 5$

Finally, for the influence of M on the pressure angle μ, while $\bar{a}_3$ and N are fixed, as Fig. 25 shows, we have:

- The higher M, the lower μ is;

- A higher M may cause low machinability or even undercutting of the ring-cam.

From eq.(23),

$$N = M \frac{a_3}{a_1 + a_3} = (i - 1) \frac{a_3}{a_1 + a_3} \tag{26}$$

That is, for a smaller pressure angle, a smaller N and a higher M are expected. On the other hand, to avoid the ring-cam profile undercutting, N cannot be too small for a given M; and M cannot be too large for a given N. For a given CDC train, when $\bar{a}_3$ and M (or N) are fixed, a large N should match a large M; on the other hand, a small N requires a small M.

For the final design, $M = 11$ is chosen, which leads to $i = 12$.

For roller No. 1, since the pressure angle is higher than 90°, to make a complicated problem reasonably simple, it is acceptable to assume that there is no contact force between the sun-cam and the roller at this condition. As Fig. 26 shows, for the given CDC train shown in Fig. 22, the values of the pressure angles μ vary w.r.t. the input angular displacement ψ of the sun-cam. The notation below is introduced for CDR trains:

- ψ_{W}: Working angle (rad);
- p_{d}: Phase difference of the working angles of two given rollers (rad);
- d: Engaging overlap, $d = \psi_{\mathrm{W}} - p_{\mathrm{d}}$ (rad);
- ϵ: Overlap ratio, $\epsilon = \psi_{\mathrm{W}} / p_{\mathrm{d}}$.

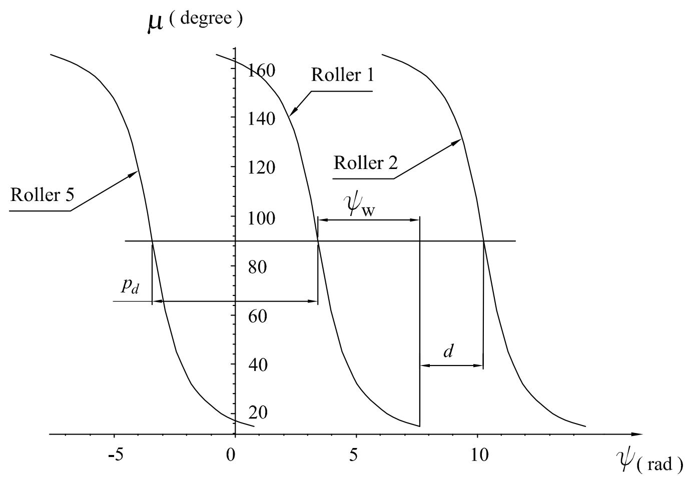

Figure 26: Pressure-angles distribution for a single-RCD CDC train

For the given CDC train, as Fig. 26 shows, the results are:

- $p_{\mathrm{d}} = 6.854384$ rad
- $\psi_{\mathrm{W}} = 4.225886$ rad
- $d = -2.628498$ rad

Notice that $d < 0$, which means that, under this condition, there is no overlap during engaging. A single RCD CDC train is thus not capable of a continuous transmission. To obtain a continuous transmission, a double-RCD CDC train is introduced, as shown in Fig. 27, while all the other structural parameters are kept unchanged. For convenience, let N_{R} represent the number of RCDs used in a CDC train. In this case, $N_{\mathrm{R}} = 2$. The relative pressure angles are shown in Fig. 28, the results being

- $p_{\mathrm{d}} = 3.427192$ rad

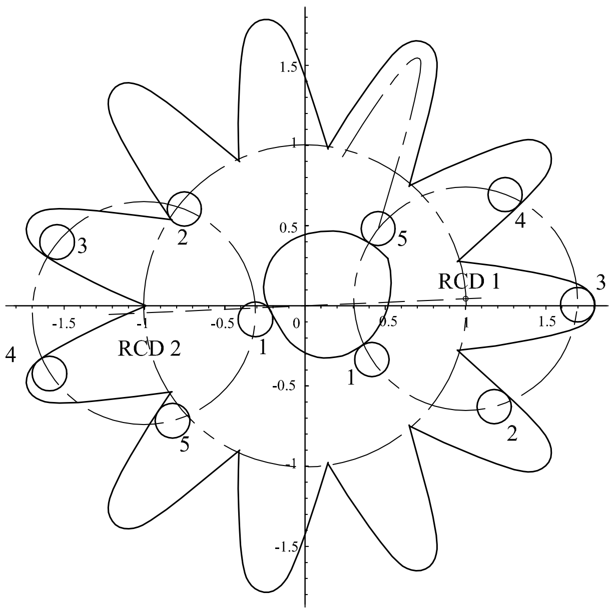

Figure 27: A double-RCD CDC train

- $\psi_W = 4.225886$ rad
- $d = 0.798668$ rad
- $\epsilon = 1.2330462$
- $\mu_{max} = 51.495631°$
- $\mu_{min} = 14.690726°$

Notice that $\epsilon > 1$, a continuous transmission then being possible. Furthermore, the working load of each roller can be expected lower. Also notice that the pressure-angle value μ_{min} at the end of engaging stage, and at the beginning stage of the overlap, μ_{max}, are two important parameters to assess the transmission. The lower the two values,

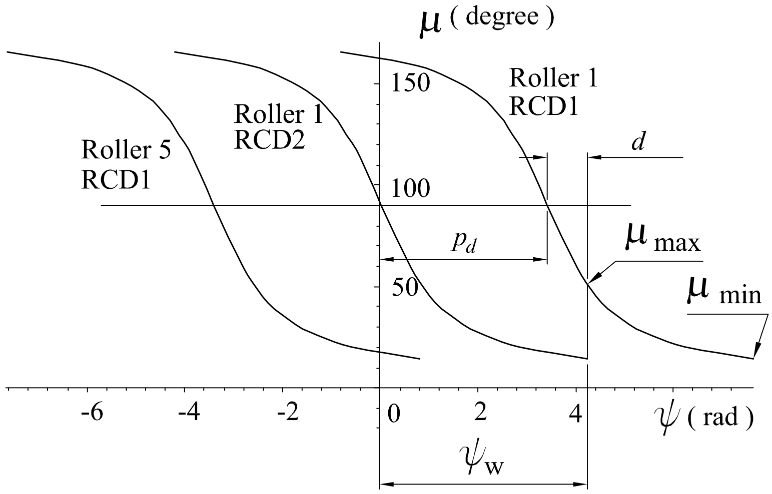

Figure 28: Pressure-angles distribution for a double-RCD CDC train

the better the transmission is. For an even higher overlap ratio ϵ and lower μ_{max} and μ_{min}, a CDC train with three RCDs, $N_{\text{R}} = 3$, is developed, as shown in Fig. 29, without changing other parameters. For this triple-RCD CDC train, we have:

- $p_{\text{d}} = 2.284795$ rad
- $\psi_{\text{W}} = 4.225886$ rad
- $d = 1.941091$ rad
- $\epsilon = 1.849569$
- $\mu_{\text{max}} = 27.762204°$
- $\mu_{\text{min}} = 14.690726°$

When compared with the double-RCD CDC train, the overlap ratio ϵ increases dramatically and μ_{max} decreases. Notice that μ_{min} remains unchanged, which means that adding

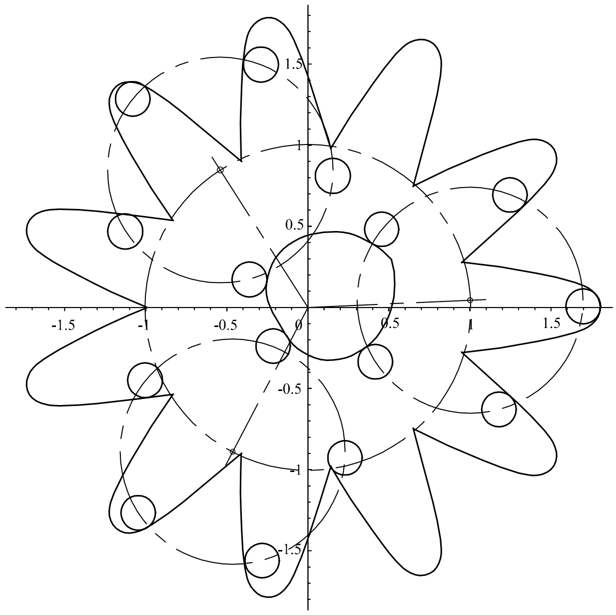

Figure 29: A triple-RCD CDC train

or reducing RCD(s) bears no influence on the pressure-angle distribution. Furthermore, the highest number of RCDs for a single sun-cam CDC train is $N_{\mathrm{R}} = 3$. In this case, four RCDs will make the parts of the mechanism interfer each other.

It is necessary to point out that the available M, or speed-reduction ratio i, for a multi-RCD CDC train is determined by the number of RCDs N_{R}. Some constraints must be observed, namely,

- i should be a multiple of N_{R};
- $M = i - 1$;
- N has no influence on N_{R}.

For example, regardless of the undercutting condition of the ring-cam:

- For a CDC train with $N_\mathrm{R} = 2$: i can be 2, 4, 6, 8, 10, 12, 14, 16, 18, 20, $\ldots$; so, $i = N_\mathrm{R} k$, k is a natural number;
- For a CDC train with $N_\mathrm{R} = 3$: i can be 3, 6, 12, 18, 24, $\ldots$; so, $i = N_\mathrm{R} k$, k is either unity or an even number.

As the synthesis and compromise of the above conditions, also taking the machinability of both the sun-cam and ring-cam into consideration, the final key parameters for the CDC train are:

- $i = 12$
- $M = 11$
- $N = 6$
- $N_\mathrm{R} = 3$
- $a_1 = 80$ mm
- $a_3 = 55$ mm
- $a_4 = 9.5$ mm

Figure 30 shows the final CDC train layout, while Fig. 31 shows the pressure angles distribution vs. the angular displacement of the sun-cam, the results being

- $p_\mathrm{d} = 2.284795$ rad
- $\psi_\mathrm{W} = 4.185983$ rad

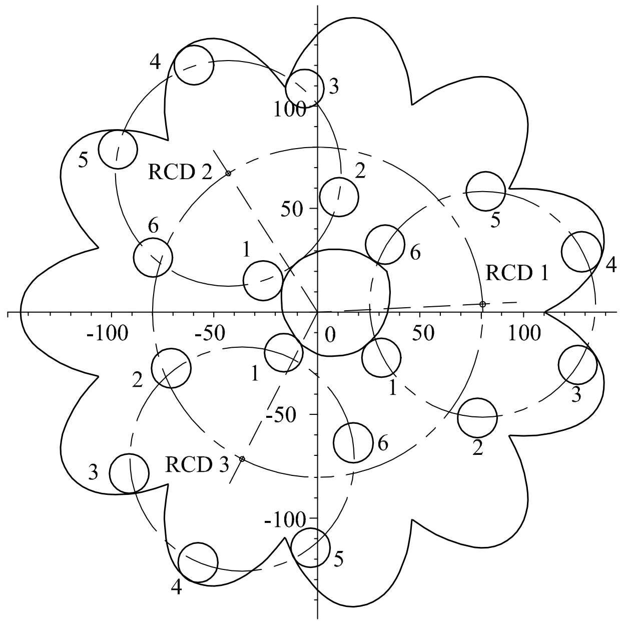

Figure 30: Alternative triple-RCD PCR train (unit: mm)

- $d = 1.901188$ rad
- $\epsilon = 1.832104$
- $\mu_{\max} = 39.177171°$
- $\mu_{\min} = 23.487010°$

Figure 32 shows the engaging sequence of the final triple-RCD CDC train. Notice that:

- At any time, there are three rollers engaging with the sun-cam;
- Only for two rollers is the pressure-angle smaller than 90°;
- There is only one roller whose pressure-angle is smaller than $\mu_{\max}$.

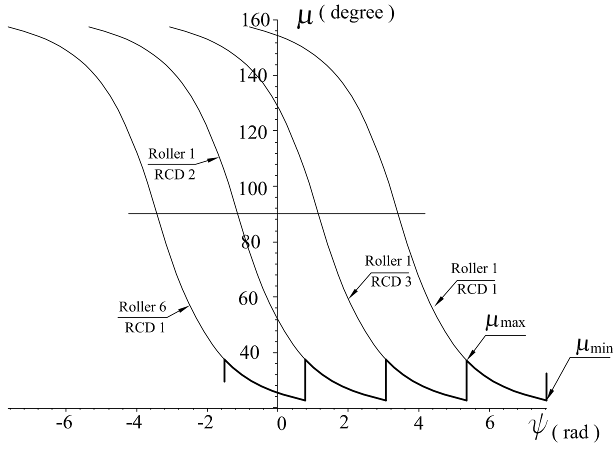

Figure 31: Pressure-angle distribution of alternative triple-RCD CDC train

5.2 Static Force Analysis

A reasonable simplifying assumption is now introduced: As the wide solid curve shows in Fig. 31, it is assumed that during the engaging of the sun-cam and the rollers at any given time, only one roller working along this curve, the pressure-angle varying between μ_{min} and μ_{max}. This means that, at any time, the whole load is taken by the roller with the smallest pressure angle. Under this assumption, the load acting on the roller can be determined. We introduce the notation below:

- i: the number of RCDs;
- j: the number of rollers of a given RCD;
- R_{ij}: the ith roller on the jth RCD;
- RCDi: the ith RCD;

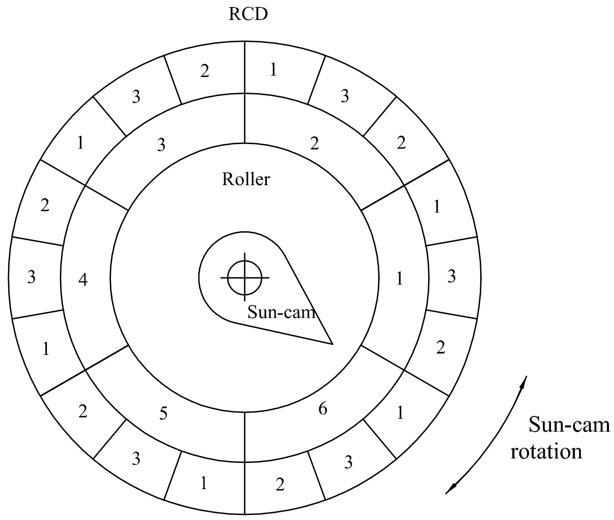

Figure 32: Engaging sequence of the alternative triple-RCD CDC train

- I_{CRi}: the instant centre of the RCDi w.r.t. the sun-cam;
- O_{ICi}: the instant centre of RCDi w.r.t. the ground;
- R_{ij}: the ith roller on the jth RCD;
- F_{ij}: the contact force acting on the centre of engaging roller R_{ij};
- V_{ij}: the speed of the centre of the engaging roller R_{ij};
- μ_{ij}: the pressure-angle of the roller R_{ij};
- F_l: the force acting on the RCD centre.

Firstly, consider the contact force between the sun-cam and the engaging rollers. For the configuration displayed in Fig. 33, and with reference to Fig. 31, the roller that engages with the sun-cam is only roller R_{16}, and the contact force is F_{16}. For other rollers and

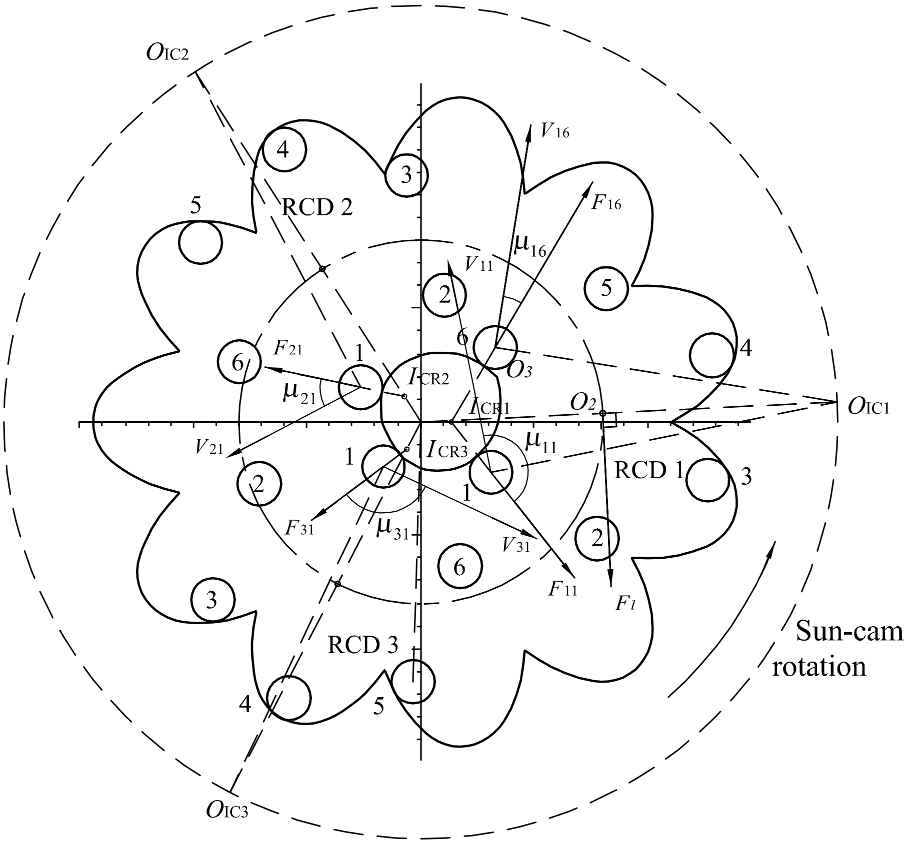

Figure 33: Force analysis of sun-cam and rollers

their contact forces, they can be overlooked under the above assumption.

Then, consider the contact force between the engaging roller and the corresponding lobe of the ring-cam. As shown in Fig. 34, by fixing the PCA, and letting the ring-cam be the driving element, the forces between the ring-cam and the rollers can be computed. Notice that, if μ_{ij} is equal to or higher than 90°, then the contact force between R_{ij} and the lobe can be overlooked. Thus, we have the following contact forces: F_{14}, F_{25}, F_{34} and F_{35} with their pressure angles less than 90°. Notice that the pressure-angle of R_{34} is near 90°, F_{34} thus contributing little to the motion of RCD3, and hence can be overlooked.

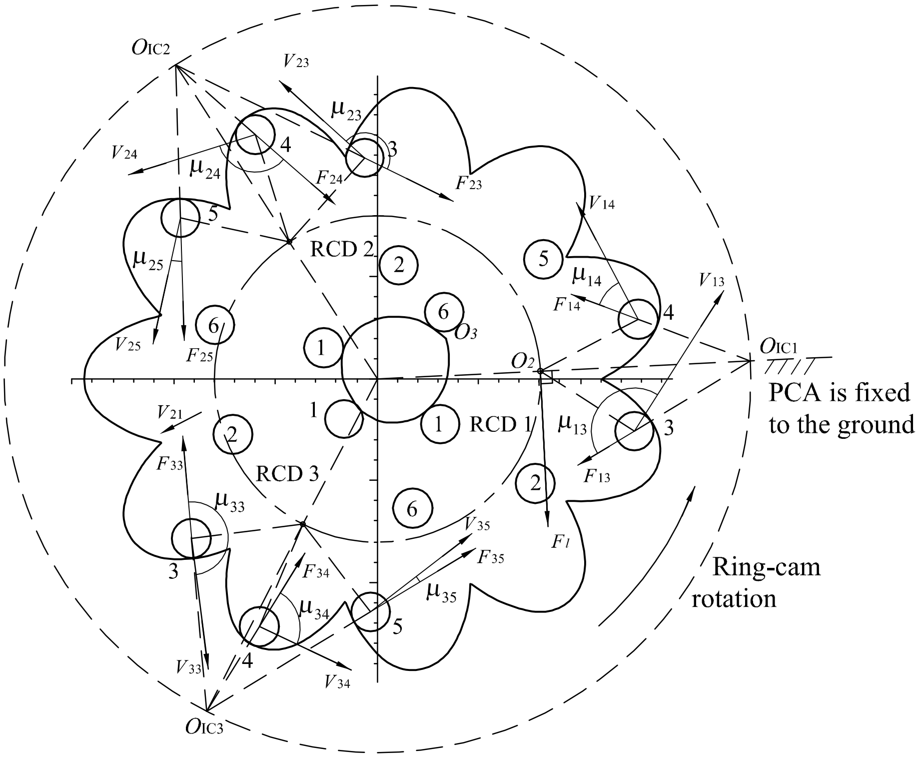

Figure 34: Force analysis of ring-cam and rollers

Furthermore, since for this configuration, only R_{16} takes the whole load, only RCD1 is the working RCD, and hence F_{25} and F_{35} can also be overlooked. For the working RCD1, as shown in Fig. 35, there are three forces acting on RCD1 now, namely:

- the driving force F_{16};
- the constraint force F_{14}; and
- the load F_l.

Hence, these three forces must be balanced, as shown in the triangle of Fig. 35. If the input power and output power are known, and the speed-reduction ratio is also known,

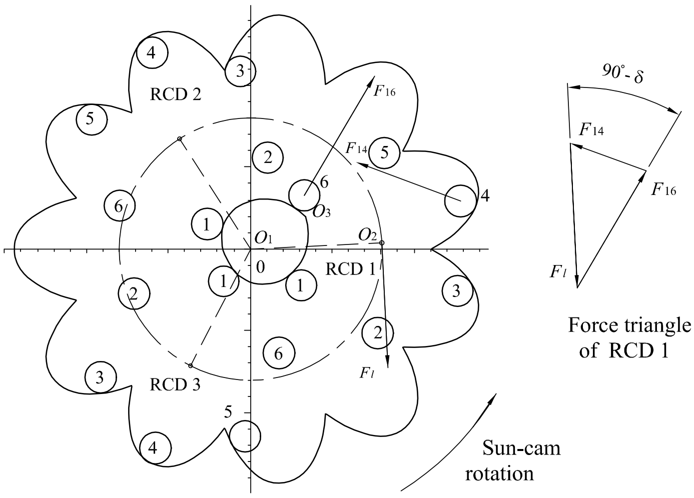

Figure 35: Final PCR train workload analysis

F_{16} and F_l can be readily found. Then, since δ can be obtained from eq.(10c), the constraint force F_{14} can also be obtained. Figure 36 shows, for a unit torque input, the variation of F_{16} and F_{14} w.r.t. ψ. Furthermore, Fig. 37 shows the ratio of F_{16}/F_{14} varying

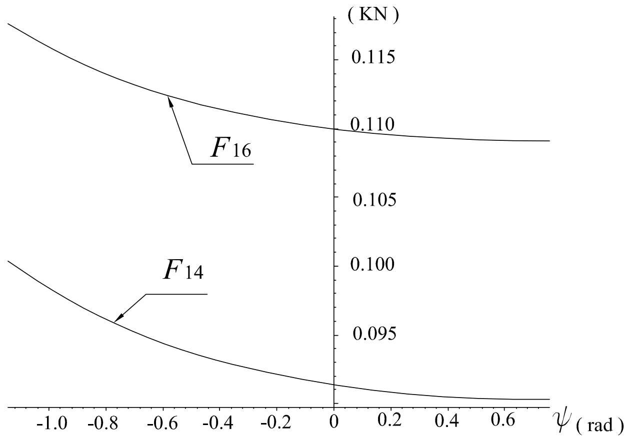

Figure 36: Distribution of F_{14} and F_{16}

vs. the angular displacement ψ. It is apparent from these plots that the highest ratio of

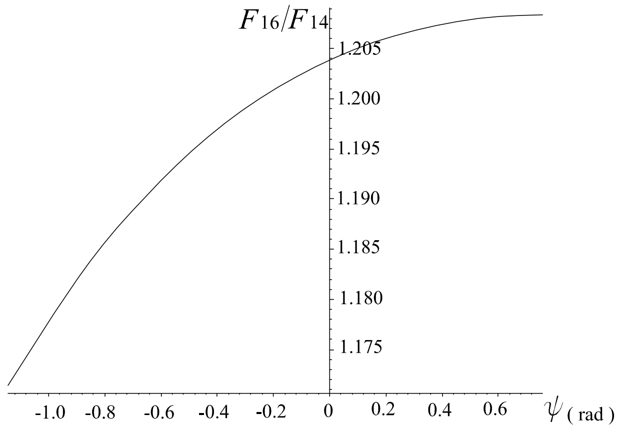

Figure 37: Distribution of force ratio F_{16}/F_{14}

F_{16}/F_{14} is 1.208 during each working cycle for any given roller.

As Fig. 38 shows, if the input torque is $M_{\rm in}$ and the output torque is $M_{\rm out}$, and assuming a transmission efficiency of the CDC train of 100%, then, the output/input torque ratio $R_{\rm M}$ can be obtained, as discribed below:

First, notice that

$$M_{\rm in} = F_{16} b_2 \sin\delta \tag{27}$$

Considering the torque balance of RCD1 w.r.t. the instant centre $O_{\rm IC}$, and noticing that the contact forces F_{13} and F_{14} pass through $O_{\rm IC}$:

$$F_{16}\cos\mu\overline{O_3O}_{\rm IC} = F_{16}\overline{O_{\rm p}O}_{\rm IC} = F_l\overline{O_2O}_{\rm IC} \tag{28a}$$

Notice that:

$$\overline{O_{\rm p}O}_{\rm IC} = \overline{I_{\rm CR}O}_{\rm IC}\sin\delta \tag{28b}$$

$$F_{16}\overline{I_{\rm CR}O}_{\rm IC}\sin\delta = F_l\overline{O_2O}_{\rm IC}$$

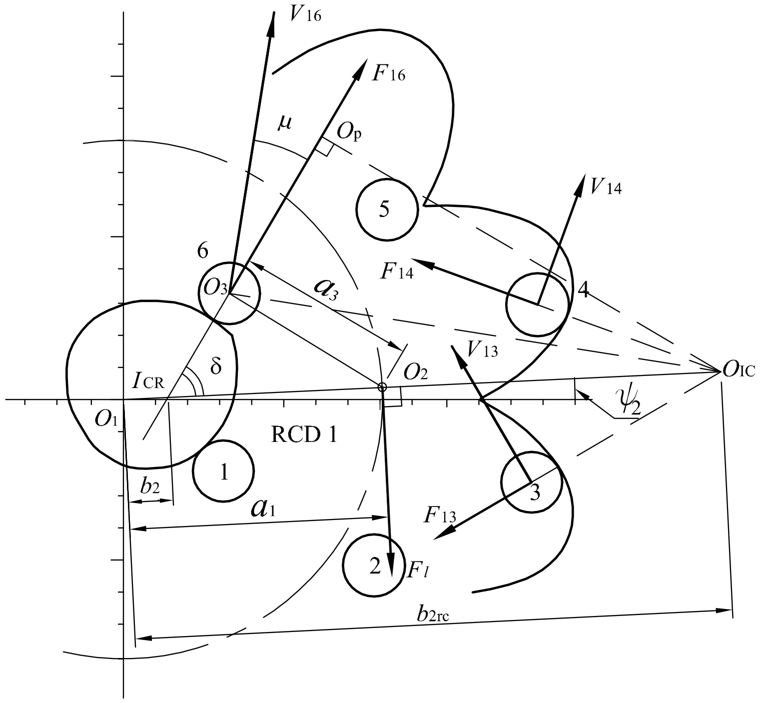

Figure 38: Final CDC train input and output torque analysis

$$F_{16}\left(b_{2\mathrm{rc}}-b_2\right)\sin\delta = F_l\left(b_{2\mathrm{rc}}-a_1\right)$$

$$F_l = \frac{F_{16}\left(b_{2\mathrm{rc}}-b_2\right)\sin\delta}{\left(b_{2\mathrm{rc}}-a_1\right)} \tag{28c}$$

The output torque M_{out} is given out as

$$M_{\mathrm{out}} = F_l\overline{O_1O_2} = F_l a_1 \tag{29}$$

The output/input torque ratio R_{M} is, then, from eqs.(27), (28) and (29),

$$R_{\mathrm{M}} = \frac{M_{\mathrm{out}}}{M_{\mathrm{in}}} = \frac{a_1\left(b_{2\mathrm{rc}}-b_2\right)}{b_2\left(b_{2\mathrm{rc}}-a_1\right)} \tag{30}$$

Furthermore, from eqs.(21), (22) and (23),

$$R_{\mathrm{M}} = M+1 = i \tag{31}$$

which is the expected result.

6 Mechanical Design of the CDC Train

6.1 Design Specifications

The design specifications of the CDC train are listed below:

Power and speed:

- Speed-reduction ratio (i): 12;
- Maximum input power (Song, 2002) : 1.0 kw at 1500 rpm.

Key mechanism parameters:

- Number of the sun-cams: 1;
- Number of lobes of the ring-cam (M): 11;
- Number of rollers per RCD (N): 6;
- Number of RCDs (N_{R}): 3.

Geometric dimensions:

- Radius of the pitch circle of the RCD (a_3): 55 mm;
- Radius of the pitch circle of the PCA (a_1): 80 mm;
- Radius of the rollers of the RCD (a_4): 9.5 mm.

Accordingly, a prototype CDC train is designed with:

- Overall hight: 350 mm;
- Overall length: 340 mm;
- Overall width: 212 mm.

6.2 Material Selection

With regard to the machined parts, we have two distinct materials, aluminium alloy and steel, as described below.

Aluminium alloys: 6061-T6

Selected for the cases, covers, sleeves, RCD as well as parts of PCA and others. Material selection was based on various reasons:

- light weight but high strength and load capacity, as compared with steel, brass or copper;
- highly machinable, as compared with steel or composites;
- good stiffness;
- readily accepts a wide range of surface finishes and resists corrosion;
- available in a wide range of sizes, shapes and forms.

Carbon steel: AISI 4140

Selected for the roller shafts, RCDs, PCA and nonstandard bolts. This material was also chosen for the sun-cam and the ring-cam. Friction of the cam surface is not an issue, because of the rollers. Further considerations pertain to contact strength and hardness. AISI 4140 with induction-hardening treatment (Minimum HRC52) can satisfy the requirements when it is used as the material for cams.

6.3 Sun-Cam Shaft Balance

In Following the method proposed by Lee (2001), the sun-cam shaft is statically and dynamically balanced, as shown in Fig 39.

However, the added balance mass dramatically increases the machining complexity,

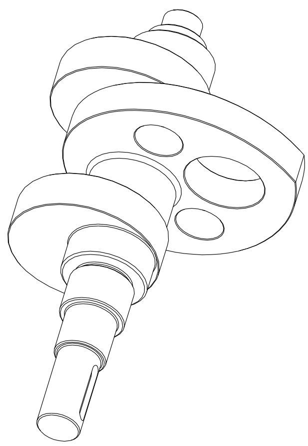

Figure 39: Mass balanced sun-cam shaft

thereby increasing its cost. A new balance method is introduced here: the counterbalances are replaced by four holes filled with lead. Figure 40 illustrates the balanced

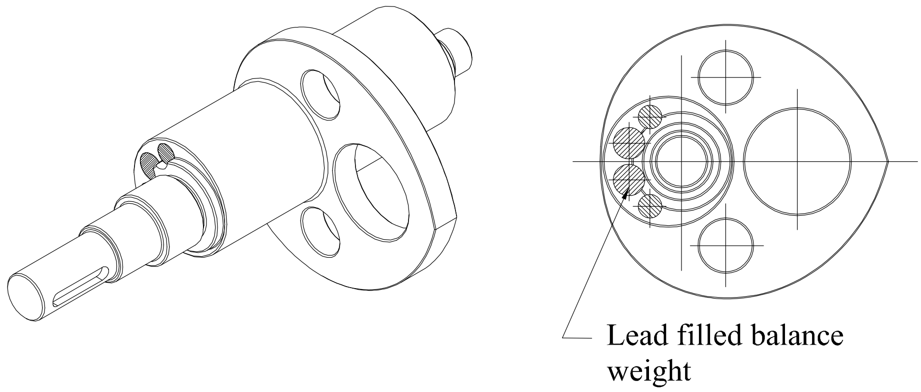

Figure 40: Balanced sun-cam shaft with filled lead

shaft. also, Detailed drawings are included in the Appendix for reference.

6.4 Bill of Materials (BOM)

The bill of materials(BOM) for the CDC train is outlined below:

The whole assembly of the CDC trains can be divided into four sub-assemblies:

- RCD;
- PCA;
- Case;
- Cam shaft;

The bill of materials appears in Tables. 5, 6, 7 and 8 in the Appendix. The materials for no-standard parts and the specifications for standard parts are also given. Moreover, for the designed parts, the drawing numbers are listed in these tables.

The final design of a CDC train prototype, implemented in Pro/Engineer, is shown in Fig. 41.

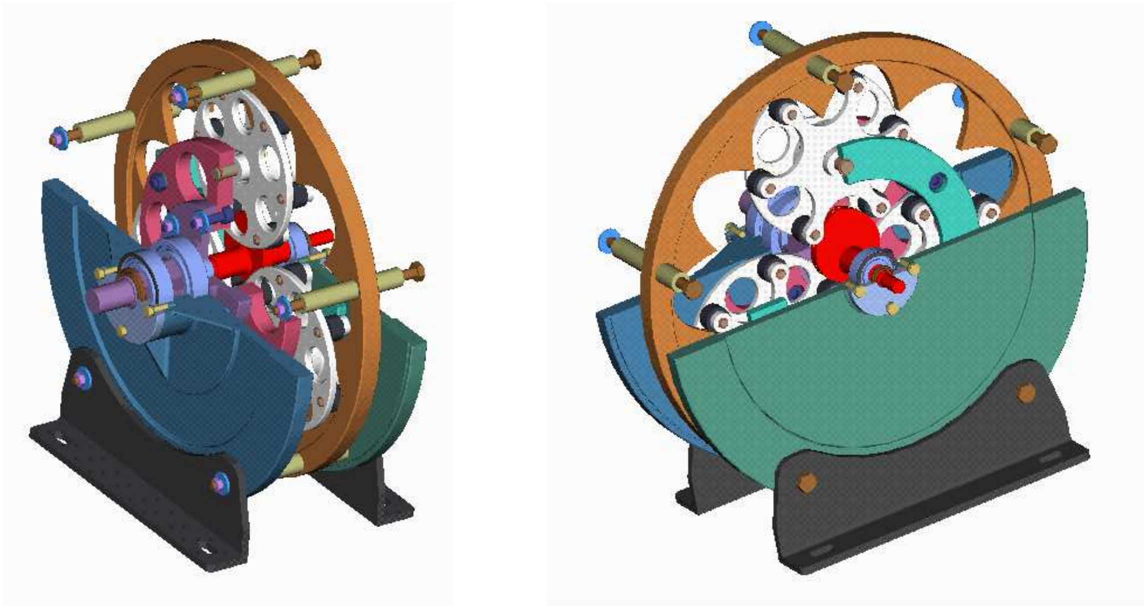

(a) (b)

Figure 41: Prototype of a CDC train unit produced with Pro/Engineer: (a) Cut view of the left side (b) Cut view of the right side

7 Failure Analysis

The reference for this section are (Edwards and McKee, 1991; Spotts and Shoup, 1998). Moreover, all calculations are based on an angular velocity $n = 1,500$ rpm.

7.1 Work Load

For a transmitted power of $P = 1,000$ watt, the input torque is

$$\tau = \frac{60P}{2n\pi} = 6.37 \text{ Nm} \tag{32}$$

where

$P = 1,000$ watt is the total power transmitted, while $n = 1,500$ rpm is the angular velocity of the cam shaft.

The contact force between rollers and sun-cam is:

$$F = \frac{\tau}{b_2 \sin\delta} = 1.115 \text{ kN} \tag{33}$$

Notice here that $\sin\delta = 0.5$ was used in the calculation, because during the effective engagement range, when μ changes from μ_{max} to μ_{min}, δ varies, roughly, between 40° and 60°. For safety purposes, $\delta = 30°$ was chosen.

The work load of the RCD shaft is:

$$F_1 = \frac{M_{\text{out}}}{a_1} = 955 \text{ kN} \tag{34}$$

7.2 Roller-Shaft Failure Analysis

For shaft failure analysis, we use the design inequality (Spotts and Shoup, 1998).

$$(\sigma_{ave} + \sigma_r K_{fb}(\frac{S_{yp}}{S_e}))^2 + 3(\tau_{ave} + \tau_r K_{ft}(\frac{S_{yp}}{S_e}))^2 \leq (\frac{S_{yp}}{N_{fs}})^2 \tag{35}$$

in which

σ_{ave} : average stress;

σ_r : range stress;

K_{fb} : fatigue stress concentration factor for bending;

τ_{ave} : average shear stress;

τ_r : range shear stress;

K_{ft} : fatigue shear concentration factor for torsion;

N_{fs} : safety factor;

S_{yp} : yield stress;

$S_{yp} =$ 95 ksi or 655.00 MPa: tension yield strength for AISI 4140;

S_e : fatigue endurance limit in pure bending;

$S_e =$ 50 ksi=344.74 MPa: endurance limit in pure bending for AISI 4140.

Moreover, the maximum stress σ due to bending is calculated as

$$\sigma = \frac{d}{2}\frac{M}{I} \tag{36}$$

where

$$I = \frac{\pi d^4}{64} \tag{37}$$

is the moment of inertia of the cross section, M is the bending moment at the section, and d is the diameter of the cross section.

Similarly, for the shear stress τ, we have

$$\tau = \frac{d}{2}\frac{T}{J} \tag{38}$$

where

$$J = \frac{\pi d^4}{32} \tag{39}$$

is the polar moment of inertia for a given shaft section, T is the torque at the cross section and d is the section diameter.

For the case of a roller shaft, we refer to Fig. 42, where:

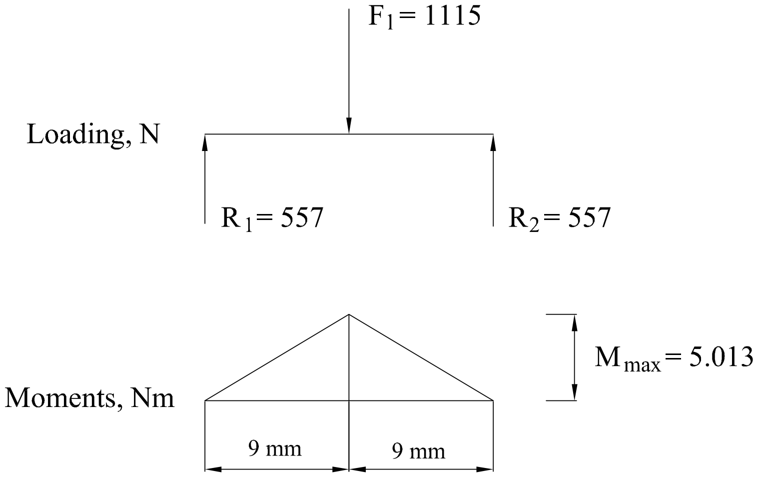

Figure 42: Loading and moment of roller shaft

$d = 6$ mm; $R_1 = R_2 = 557$ N; $M_{max} = 5,013$ Nmm; $T = 0$ Nmm; $I = 63.58$ mm^4; $J = 127.17$ mm^4.

Moveover, $\sigma_{max} = 236.54$ MPa; $\sigma_{ave} = \sigma_{max}/2 = 118.27$ MPa; $\sigma_r = \sigma_{max}/2 = 118.27$ MPa; $K_{fb} = 1.00$; $\tau_{ave} = 0$ MPa; $\tau_r = 0$ MPa; $K_{ft} = 1.00$; $N_{fs} = 1.8$.

Substituting the above data into eq.(35) yields a value of $117,635.93$ MPa^2 for the left-hand side, which is smaller than the value of $132,415.12$ MPa^2 of the right-hand side of the same inequality, and hence, the design is safe.

7.3 RCD Shaft Failure Analysis

For the RCD shaft, since the input rotational speed is 1500 rpm, the mass of the RCD is 1.014 kg. We have a centrifugal force C_t per RCD given by

$$C_t = m\omega^2 r \tag{40}$$

where $m = 1.014$ kg; $\omega = 13.09$ s^{-1}; and $r = 0.08$ m. Therefore, $C_t = 13.89$ N.

The total load of the RCD shaft is then

$F_t = \sqrt{C_t^2 + F_l^2} = 955.1$ N

From the static analysis of Fig. 43,

$R_1 = R_2 = 477.5$ N; $M_{max} = 13,370$ Nmm; $T = 0$ Nmm; $d = 10$ mm; $J = 981.25$ mm^4; $I = 490.63$ mm^4; $\sigma_{ave} = 51.09$ MPa; $\sigma_r = 0$ MPa; $K_{fb} = 1.00$; $\tau_{ave} = 0$ MPa; $\tau_r = 0$ MPa; $K_{ft} = 1.00$; $N_{fs} = 2$.

Substituting the above data into eq.(35) yields a value of $2,610.19$ MPa^2 for the left-hand side, which is smaller than the value of $107,256.25$ MPa^2 of the right-hand side, and hence, the design is safe.

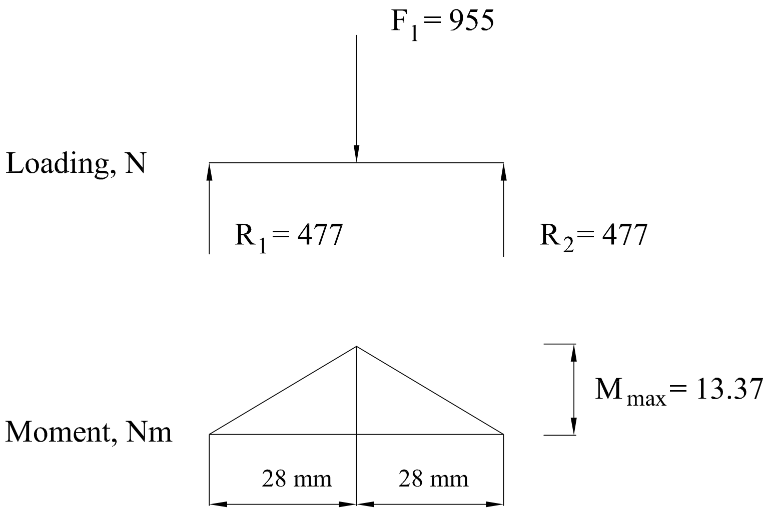

Figure 43: Loading and moment of RCD shaft

7.4 PCA Shaft Failure Analysis

The output torque is $\tau_{out} = 12\tau_{in} = 76.44$ Nm, and the work load is $F_l = 955$ N.

As shown in Fig. 44, $R_1 = 2,832$ N; $R_2 = 1,877$ N; $M_{max} = 54,433$ Nmm; $T = 76,440$ Nmm; $d = 20$ mm; $J = 15,700$ mm^4; $I = 7,850$ mm^4; $\sigma_{ave} = 69.34$ MPa; $\sigma_r = 0$ MPa; $K_{fb} = 2.2$; $\tau_{ave} = 48.69$ MPa; $\tau_r = 0$ MPa; $K_{ft} = 1.85$; $N_{fs} = 2$.

Substituting the above data into eq.(35) yields a value of $11,920.18$ MPa^2 for the left-hand side, which is smaller than the value of $107,256.25$ MPa^2 of the right-hand side, and hence, the design is safe.

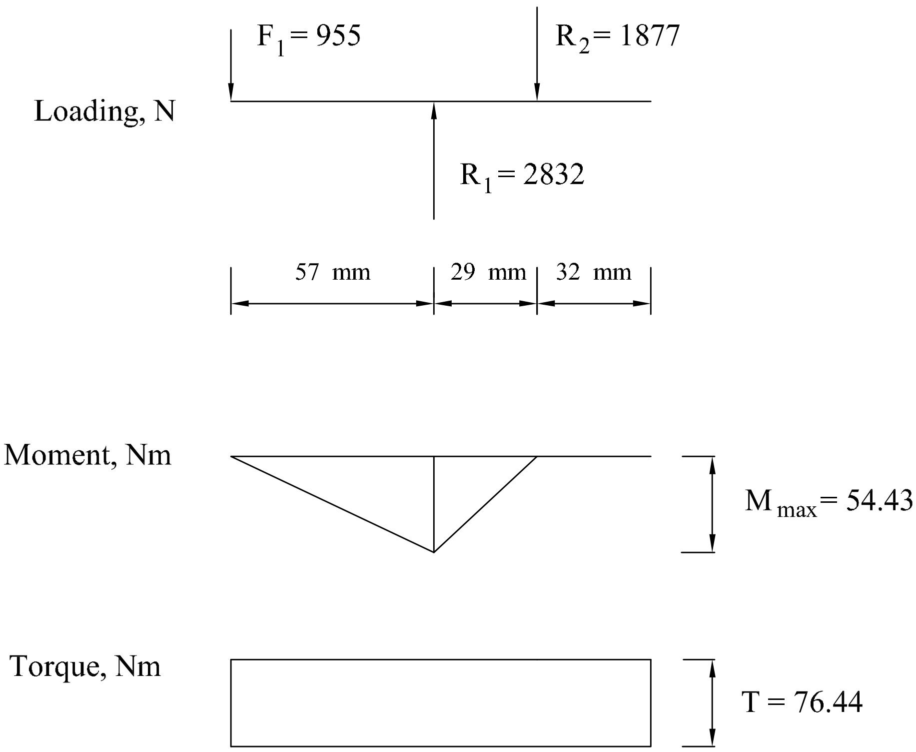

Figure 44: Loading and moment of the PCA shaft

7.5 Cam shaft Failure Analysis

The input torque is $\tau_{in} = 6.37$ Nm, and the work load is, $F_l = 1,115$ N.

As shown in Fig. 45, $R_1 = 557$ N; $R_2 = 557$ N; $M_{max} = 21,723$ Nmm; $T = 6,370$ Nmm; $d = 10$ mm; $J = 981.25$ mm^4; $I = 490.63$ mm^4; $\sigma_{ave} = 221.38$ MPa; $\sigma_r = 22$ MPa; $K_{fb} = 2.0$; $\tau_{ave} = 389.50$ MPa; $\tau_r = 0$ MPa; $K_{ft} = 1.85$; $N_{fs} = 2$.

Substituting the above data into eq.(35) yields a value of $98,985.14$ MPa^2 for the left-hand side, which is smaller than the value of $107,256.25$ MPa^2 of the right-hand side, and hence, the design is safe.

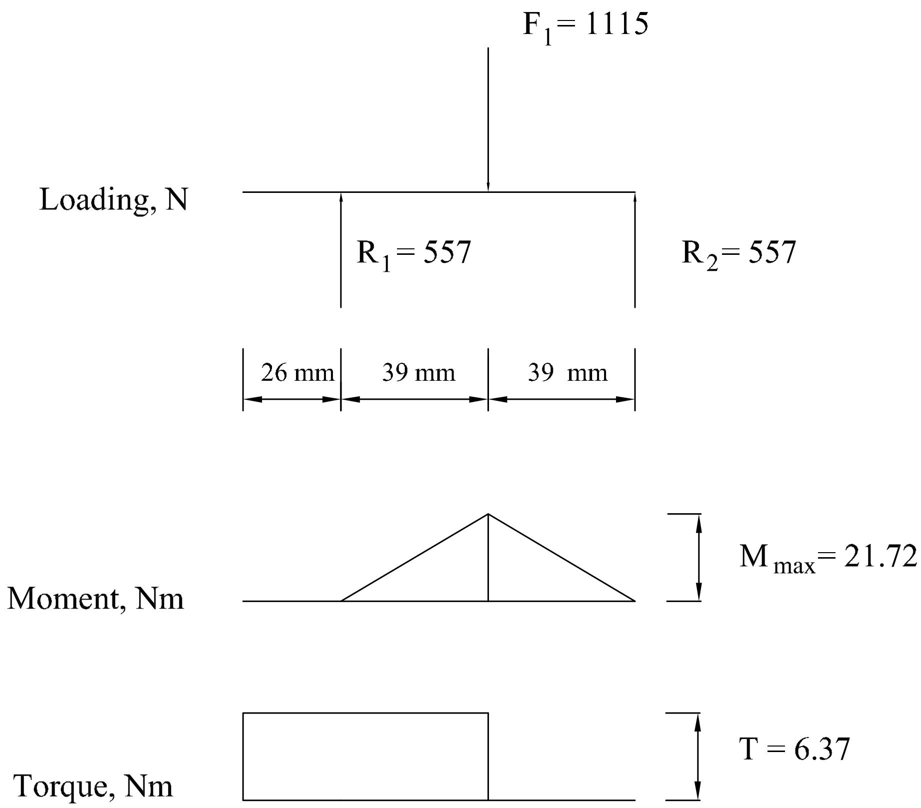

Figure 45: Loading and moment of cam shaft

7.6 Fatigue Life for Bearings

Here we refer to (Norton, 2002), in which the calculations are based.

For ball bearings,

$$L = \left(\frac{C}{P}\right)^{3} \tag{41}$$

while, for roller bearings,

$$L = \left(\frac{C}{P}\right)^{\frac{10}{3}} \tag{42}$$

where,

L : fatigue life expressed in millions of revolutions;

P : the applied load, N;

C : the basic dynamic load rating defined in bearing catalogues, N.

We also assume that this speed reducer will be working 6 hours per day, 300 days per year.

7.6.1 Cam Shaft Bearing

For the cam shaft, ball bearings 699 and 6202 are chosen. For ball bearing 699, according to the INA CANADA INC. catalogue,

Dynamic load capacity: 1,710 N;

Static load capacity: 740 N.

From Section 7.5, the maximum static load of this bearing will be 557 N, smaller than 740 N, so that the static load capacity of this bearing is acceptable. Moreover, according to eq.(41), we have,

$L = (1,710/557)^3 = 28.9 \times 10^6$ revolutions, which amounts to

$h = 28.9 \times 10^6/(1,500 \times 60) \approx 321$ h.

For ball bearing 6202, according to the INA CANADA INC. catalogue,

Dynamic load capacity: 7,700 N,

Static load capacity: 3,500 N,

From Section 7.5, the maximum static load of this bearing will be 557 N, smaller than 3,500 N, so that the static load of this bearing is acceptable. Furthermore, according to eq.(41), we have,

$L = (7,700/557)^3 = 2,641 \times 10^6$ revolutions, which amounts to

$h = 2,641 \times 10^6/(1,500 \times 60) \approx 29,344$ h.

7.6.2 PCA Shaft Bearing

For the PCA shaft, ball bearings 6006 and 6007 are chosen. For ball bearing 6006, according to the INA CANADA INC. catalogue,

Dynamic load capacity: 13,200 N;

Static load capacity: 8,300 N.

From Section 7.4, the maximum static load of this bearing will be 1,877 N, smaller than 8,300 N, so that the static load of this bearing is acceptable. According to the speed reduction ratio, the PCR speed is 125 rpm. According to eq.(41), we have, $L = (13,200/1,877)^3 = 347.79 \times 10^6$ revolutions, which amounts to

$h = (347.79 \times 10^6)/(125 \times 60) \approx 46,356$ h.

For ball bearing 6007, according to the INA CANADA INC.catalogue,

Dynamic load capacity: 16,000 N;

Static load capacity: 10,300 N.

From Section 7.4, the maximum static load of this bearing will be 2,832 N, smaller than 10,300 N, so that the static load of this bearing is acceptable. according to the speed reduction ratio, the PCR speed is 125 rpm. According to eq.(41), we have,

$L = (16,000/2,832)^3 = 175.6 \times 10^6$ revolutions, which amounts to

$h = 175.6 \times 10^6/(125 \times 60) \approx 23,412$ h.

7.6.3 RCD Shaft Bearing

For the RCD shaft, ball bearing 6000 is chosen, for which, according to the INA CANADA INC. catalogue,

Dynamic load capacity: 4,600 N;

Static load capacity: 1,950 N;

From Section 7.3, the maximum static load of this bearing will be 955 MPa, smaller than 1,950 N, so that the static load of this bearing is acceptable. According to eq.(8), the RCD speed is 229.2 rpm, while, according to eq.(41), we have

$L = (4,600/955)^3 = 111.6 \times 10^6$ million revolutions, which amounts to

$h = 111.6 \times 10^6/(229.2 \times 60) \approx 486,910$ h.

7.6.4 RCD Cam Follower

For the cam followers, NATR6 bearings are chosen, for which, according to the INA CANADA INC. catalogue, Dynamic load capacity: 4,250 N;

Static load capacity: 4,600 N;

From Section 7.2, the maximum static load of this follower is 1,115 N, smaller than 4,600 N, the static load of this bearing thus being acceptable.

The maximum speed of the cam follower can be calculated by resorting to Fig. 46, with reference to Sections 3 and 4. According to this figure,

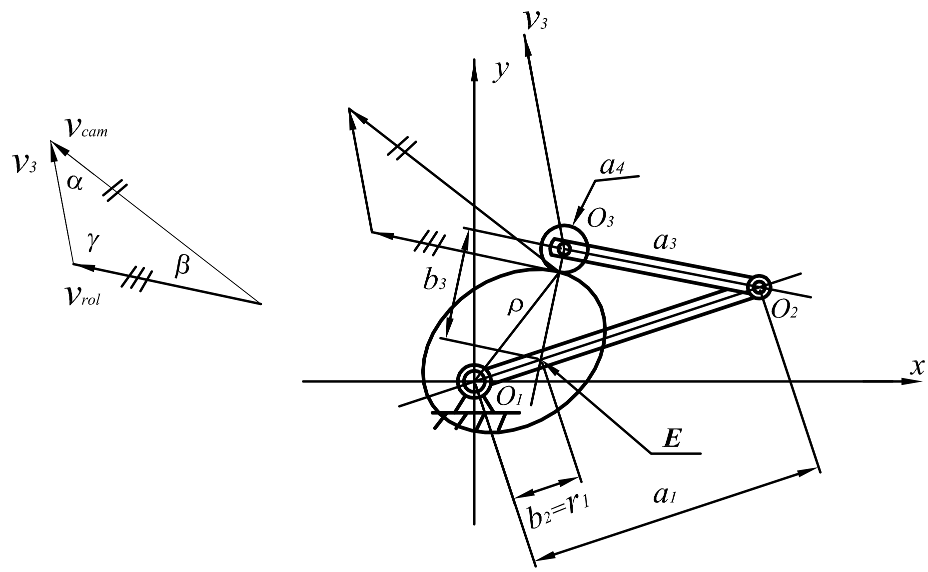

Figure 46: Cam follower angular velocity calculation

$$\overline{O_1O}_{\mathrm{IC}} = \frac{a_1 M}{(M - N)} \tag{43}$$

$$r_2 = \frac{(\overline{O_1O}_{\mathrm{IC}} - b_2)}{2} \tag{44}$$

$$d_{\mathrm{f}} = r_2 + b_2 - a_1 \tag{45}$$

$$\overline{O_3 O}_{\mathrm{IC}} d_{\mathrm{f}} = \sqrt{a_3^2 + (d_{\mathrm{f}} + r_2)^2 - 2a_3(d_{\mathrm{f}} + r_2)\cos\tilde{\phi}_1} \tag{46}$$

$$\beta = \delta - \arctan(\frac{(b_3 - a_4)\sin\delta}{(b_3 - a_4)\cos\delta + b_2}) \tag{47}$$

$$\rho = \sqrt{(b_2 + (b_3 - a_4)\cos\delta)^2 + ((b_3 - a_4)\sin\delta)^2} \tag{48}$$

where ρ is the distance from the engaging point to the centre of the cam. Moreover,

$$\omega_{\mathrm{cam}} = 50\pi \ \mathrm{s}^{-1} \tag{49}$$

which is the speed of the cam, and

$$V_{\mathrm{cam}} = \frac{\rho\omega_{\mathrm{cam}}}{1000} \ \mathrm{m/s} \tag{50}$$

is the speed of the engaging point on the cam. Furthermore,

$$V_{\mathrm{I}} = b_2\omega_{\mathrm{cam}}/1000 \ \mathrm{m/s} \tag{51}$$

$$V_3 = \frac{V_{\mathrm{I}}\overline{O_3 O}_{\mathrm{IC}}}{a_1 - b_2 + d_{\mathrm{f}} + r_2} \tag{52}$$

$$\gamma = \pi + \arctan\left(\frac{dV}{dU}\right) \tag{53}$$

$$\alpha = \pi - \gamma - \beta \tag{54}$$

The speed difference between V_{cam} and V_3 is

$$V_{\mathrm{rol}} = \sqrt{V_3^2 + V_{\mathrm{cam}}^2 - 2V_3 V_{\mathrm{cam}}\cos\alpha} \tag{55}$$

while the speed of follower is

$$\omega_{\mathrm{rol}} = \frac{1000V_{\mathrm{rol}}}{a_4}\ \mathrm{s}^{-1} \tag{56}$$

and that of cam follower is

$$n_{\mathrm{rol}} = \frac{30\omega_{\mathrm{rol}}}{\pi}\ \mathrm{rpm} \tag{57}$$

After calculation, the maximum speed of the cam follower is 5,500 rpm. According to eq.(42), we have:

$L = (4,250/1,115)^{(10/3)} = 86.5 \times 10^6$ revolutions, or

$h = 86.5 \times 10^6/(229.2 \times 60) = 6,295$ h.

7.7 Contact Analysis of the Sun-Cam and Followers

7.7.1 Static Contact Analysis

According to Fig. 37, the contact force between the sun-cam and followers is higher than that between the ring-cam and followers. So, only the contact strength of the sun-cam is verified here. For this part of the calculation, we refer to (Norton, 2002). The work load F_{l}, from eq.(33), is $F_{\mathrm{l}} = 1,115$ N. Moveover, the maximum contact pressure is

$$P_{\max} = \frac{2F_{\mathrm{l}}}{\pi a L} \tag{58}$$

where:

L is the contact length, equal to the actual contact width of the cam, namely, $L =$

$8 - 0.6 = 7.4$ mm, and a is the contact-region half-width. Moveover, the average pressure is the applied force divided by the contact-region area $P_{\mathrm{ave}} = F_{\mathrm{l}}/2aL$, while, for the contact region, $b = (1/R_1 + 1/R_2)/2$, where R_1 is the radius of the cam follower, 9.5 mm. Moveover, R_2 is the minimum radius of curvature of the cam profile (Lee, 2001); in our case, R_2 is 22.276 mm, so that $b = 75.073\ \mathrm{m}^{-1}$. Furthermore, a is obtained from

$$a = \sqrt{\frac{2}{\pi}\frac{m_1 + m_2}{B}\frac{F_l}{L}} \tag{59}$$

where, $m_1 = (1-\nu_1^2)/E_1$ and $m_2 = (1-\nu_2^2)/E_2$, in which, E_1, E_2 and ν_1, ν_2 are the Young moduli and the Poisson ratios for cam-follower and sun-cam, respectively. For E_1 and E_2, we take the same value of 2.07×10^{11} Pa, while, for ν_1 and ν_2, we take the same value of 0.3, then we have $m_1 = m_2 = 4.396 \times 10^{-12}\ \mathrm{m}^2/\mathrm{N}$. Accordingly, $a = 1.060 \times 10^{-4}$ m. Thus, for the average and maximum contact stresses, we have:

$P_{\mathrm{ave}} = 711$ MPa and $P_{\mathrm{max}} = 905$ MPa.

The maximum normal stress at the centre of the contact region is given by $\sigma_{\mathrm{z_{max}}} = \sigma_{\mathrm{x_{max}}} = -P_{\mathrm{max}} = -905$ MPa.

According to the maximum normal stress theories of failure, since $|\sigma_{\mathrm{z_{max}}}| = 905$ MPa is smaller than $S_{yt} = 1,740$ MPa (for AISI 4140, oil quenched and tempered), the static contact stress is acceptable.

8 Conclusions

The kinematic analysis and the design of a epicyclic (planetary) cam-roller train, in the configuration of cam-roller carrying disk-cam(CDC), were discussed. Regarding the kinematics of the CDC train, the concept of virtual disk (VD) was introduced for a better understanding of the relative motions of sun-cam, roller carrying disk(RCD) and ring-cam. Then, the speed-reduction ratio i was derived. Furthermore, the relations among i, the number of rollers N, the number of RCDs N_{R} and the number of lobes M of the ring-cam were derived for purposes of parameter optimization. Finally, the critical and undercutting conditions of the profile of the lobes of the ring-cam were obtained. For design purposes, the precise motion transmission and kinetostatic robustness were the main concerns. The profile of the sun-cam and ring-cam were obtained by using the method of González-Palacios and Angeles (1999). Then, the power transmission chain, pressure angle and static forces were analyzed. Based on this, the layout of the CDC train was determined, and a novel CDC train for speed reduction, with three epicyclic cam-roller trains was designed.

A prototype of the CDC train were produced for future research and development, with the purpose of static and dynamic performance evaluation.

9 References

American National Standard Engineering Drawing and Related Documentation Practices, ANSI Y14.5-1973, The American Society of Mechanical Engineers, New York.

Angeles, J., 2002, *Fundamentals of Robotic Mechanical Systems: Theory, Methods, and Algorithms*, Second Edition, Springer-Verlag, New York.

Buckingham, E., 1963, *Analytical Mechanics of Gears*, Dover Publication, Inc., New York.

Drake, P.J. 1999, *Dimensioning and Tolerancing Handbook*, McGraw-Hill, New York.

Dudley, D.W., 1991, *Handbook of Practical Gear*, McGraw-Hill, New York.

Edwards, K.S. and McKee, R.B., 1991, *Fundamentals of Mechanical Component Design*, McGraw-Hill, Inc. New York.

González-Palacios, M.A. and Angeles, J., 1993, *Cam Synthesis*, Kluwer Academic Publishers, Dordrecht, Boston.

González-Palacios, M.A. and Angeles, J., 1999, The Design of a Novel Mechanical Transmission for Speed Reduction, *J. ASME of Mechanical Design*, Vol. 121-4.

Lee, M.K., 2001, *Design for Manufacturability of Speed-Reduction Cam Mechanisms*, M.Eng., Thesis, McGill University, Canada.

Müller, H.W., 1982, *Epicyclic Drive Trains, Analysis, Synthesis, and Applications*, Wayne State University Press, Detroit.

Norton, R.L., 1999, *Design of Machinery*, Second Edition, WCB McGraw-Hill, New York.

Norton, R.L., 2002, *Cam Design and Manufacturing Handbook*, Industrial Press, New York.

Oberg, E., Jones, F.D. and Horton, H.L., 1988, *Machinery's Handbook*, 23rd Edition. Industrial Press Inc. New York.

Parnes, R., 2001, *Solid Mechanics in Engineering*, John wiley&sons, LTD. New York.

Song, X.H., 2002, *The Parameter Identification of A Novel Speed Reducer*, M.Eng., Thesis, McGill University, Canada.

Spotts, M.F. and Shoup, T.E., 1991, *Design of Machine Elements*, Prentice Hall, New Jersey.

Stock Drive Products: *Handbook of Small Standardized Components, Master Catalog 757*, New Hyde Park, New York.

Tuttle, T. and Seering, W., 1993, Kinematic Error, Compliance, and Friction in a Harmonic Drive Gear Transmission, *J. ASME Advances in Design Automation*, Vol. 65-1.

Ullman, David G. 1997, *The Mechanical Design Process*, Second Edition, McGraw-Hill, Boston, Massachusetts.

Yuen, W.K., 1996, *Dynamics and Control of a High-Rate Speed Reduction Cam Mechanism*, M.Eng., Thesis, McGill University, Canada.

10 Appendix

Part list and Drawings

Table 4: Assembly of PCR Trains Mechanism

Assembly	Sub-assembly	Sub-assembly
CDC total assembly.	PCA sub-assembly	RCD sub-assembly
		RCD sub-assembly
		RCD sub-assembly
	Cam shaft sub-assembly	
	Case sub-assembly	

Table 5: Parts list of 3 RCD Sub-assembly

Name	Specification/Index No.	Quantity	Material/Vendor
No-standard Parts			
RCD	CDC46-0-02-03-07	3	AA6061
Roller Shaft	CDC40-0-02-03-01	18	AISI 4140
RCD Shaft	CDC27-0-02-01-01	3	AISI 4140
Sleeve	CDC43-0-02-03-04	6	Nylon 66
Standard Parts			
Roller	NATR6P	18	INA
Snap ring D6	WR6	36	INA
Snap ring D10	WR10	6	INA
Ball Bearing 6000	6000	3	INA
House snapper BR26	BR26	3	INA

Table 6: Parts list of PCA sub-assembly

Name	**Specification/Index No.**	**Quantity**	**Material/Vendor**
No-standard Parts			
RCD	Sub-assembly	3	
PAD Disk Left	CDC28-0-02-01-02	1	AA6061
PAD Disk Right	CDC30-0-02-01-04	1	AA6061
PAD Shaft	CDC31-0-02-01-05	1	AISI 4140
Bolt PAD D8M6	CDC27-0-02-01-01	6	AISI 304
Standard Parts			
Ball Bearing 6006	6006	1	INA
Ball Bearing 6007	6007	1	INA
Nut M6	M6	11	BS3692:1967
Nut M8	WR6	3	BS3692:1967
Bolt M8	M8 $\times$ 55(b20)	3	BS4168:PI:1981
Spring Washer M6	M6	11	BS4464:1969
Spring Washer M8	M8	3	BS4464:1969
Plain Washer M6	M6 Form G	11	BS4320:1968

Table 7: Parts list of cam shaft Sub-assembly

Name	**Specification/Index No.**	**Quantity**	**Material/Vendor**
No-standard Parts			
Cam Shaft	CDC38-0-02-02-02	1	AISI 4140
Standard Parts			
Ball Bearing 699	699	1	INA
Ball Bearing 6202	6202	1	INA

Table 8: Parts list of Case Sub-assembly

Name	**Specification/Index No.**	**Quantity**	**Material/Vendor**
No-standard Parts			
Ring Cam	CDC15-0-01-12	1	AISI 4140
Box Left	CDC18-0-01-15	1	AA6061
Box Right	CDC12-0-01-10	1	AA6061
Cover Right	CDC11-0-01-08	1	AISI 304
Cover Left	CDC22-0-01-19	1	AISI 304
Foot	CDC07-0-01-04	2	AISI 304
Washer L Cover	CDC23-0-01-20	3	Nylon66
Washer R Cover	CDC12-0-01-09	3	Nylon66
Sleeve Left	CDC16-0-01-13	5	AA6061
Sleeve Right	CDC14-0-01-11	5	AA6061
Bolt D8M6-125	CDC20-0-01-17	3	AISI 304
Bolt D8M6-135	CDC19-0-01-16	2	AISI 304
Cover Case	CDC17-0-01-14	1	AISI 304
Standard Parts			
Bolt M5	M5 $\times$ 15L	8	BS 3692:1967
Spring Washer M5	M5	8	BS 4464:1969
Seal G12	G12 $\times$ 18 $\times$ 3AF	1	INA
Seal G25	G25 $\times$ 35 $\times$ 4AF	1	INA